

NONLINEAR SHOCK ACCELERATION AND PHOTON EMISSION IN SUPERNOVA REMNANTS

Donald C. Ellison

Department of Physics, North Carolina State University,
Box 8202, Raleigh NC 27695, U.S.A.

don_ellison@ncsu.edu

Evgeny G. Berezhko

Institute of Cosmophysical Research and Aeronomy,
Lenin Avenue 31, 677891 Yakutsk, Russia

berezhko@sci.yakutia.ru

and

Matthew G. Baring¹

Laboratory for High Energy Astrophysics, Code 661,
NASA Goddard Space Flight Center, Greenbelt, MD 20771, U.S.A.

baring@lheavx.gsfc.nasa.gov

ABSTRACT

We have extended a simple model of nonlinear diffusive shock acceleration (Berezhko & Ellison 1999; Ellison & Berezhko 1999a) to include the injection and acceleration of electrons and the production of photons from bremsstrahlung, synchrotron, inverse-Compton, and pion-decay processes. We argue that the results of this model, which is simpler to use than more elaborate ones, offer a significant improvement over test-particle, power-law spectra which are often used in astrophysical applications of diffusive shock acceleration. With an evolutionary supernova remnant (SNR) model to obtain shock parameters as functions of ambient interstellar medium parameters and time, we predict broad-band continuum photon emission from supernova remnants in general, and SN1006 in particular, showing that our results compare well with the more complete time-dependent and spherically symmetric nonlinear model of Berezhko, Ksenofontov, & Petukhov (1999a). We discuss the implications nonlinear shock acceleration has for X-ray line emission, and use our model to describe how ambient conditions determine the TeV/radio flux ratio, an important parameter for γ -ray observations of radio SNRs.

Subject headings: acceleration of particles — cosmic rays — supernova remnants — radiation mechanisms: non-thermal — gamma-rays: theory — ISM: individual (SN1006)

¹Universities Space Research Association

1. INTRODUCTION

More than twenty years of spacecraft observations in the heliosphere have proven that collisionless shocks can accelerate particles with high efficiency, i.e., 10-50% of the ram energy can go into superthermal particles (e.g., Eichler 1981; Gosling et al. 1981; Ellison et al. 1990). A recent example comes from Terasawa et al. (1999) who report on an interplanetary shock, observed by GEOTAIL, where the pressures in thermal and accelerated particles, and the magnetic field are in approximate equipartition in the foreshock. They observed that the shock transition was smoothed by the energetic particle backpressure, giving unambiguous evidence that nonlinear acceleration occurred in an interplanetary shock, weak by astrophysical standards (for this exceptionally strong interplanetary shock, the sonic Mach number was $M_{S0} \sim 5 - 10$). Energetic particles exist throughout the universe and shocks are commonly associated with them, confirming that shock acceleration is important beyond the heliosphere. In fact, shocks are believed to be the main source of Galactic cosmic rays, and energetic particles from shocks may produce spectacular events such as γ -ray bursts and X-ray and gamma-ray flaring in blazars. The shocks in these objects are expected to be much stronger than those in the heliosphere and can only be more efficient and nonlinear. The conjecture that collisionless shocks are efficient accelerators is strengthened by results from plasma simulations which show efficient shock acceleration consistent with spacecraft observations (e.g., Scholer, Trattner, & Kucharek 1992; Giacalone et al. 1997). Other indirect evidence comes from the implied efficiency of galactic cosmic ray production, radio emission from supernova remnants (SNRs) (see Reynolds & Ellison 1992), equipartition arguments in AGNs and γ -ray bursts, etc. (see Blandford & Eichler 1987 for an early review). There is also clear evidence that shocks can produce strong self-generated turbulence. This has long been seen in heliospheric shocks (e.g., Lee 1982, 1983; Kennel et al. 1984; Baring et al. 1997) and there is evidence that it occurs at SNRs as well (i.e., Achterberg, Blandford, & Reynolds 1994).

Despite this compelling evidence for efficient, nonlinear shock acceleration, many astrophysical applications of shock acceleration continue to use the test-particle theory proposed more than 20 years ago by Axford, Leer, & Skadron (1977), Krymskii (1977), Bell (1978), and Blandford & Ostriker (1978). We believe it is possible that test-particle models are used in situations where nonlinear shocks are clearly expected because the numerical, nonlinear results are complicated and unwieldy. None of the current techniques modeling nonlinear shocks have simple analytic approximations and this makes it difficult to perform parameter searches or compare nonlinear results to observations.

Here, in an attempt to remedy this situation, we present a simple model of diffusive shock acceleration, based on more complete studies, which includes the essential physics of nonlinear acceleration when the backpressure from energetic ions modifies the shock structure and induces spectral curvature. This model is computationally fast and easy-to-use, but complete enough to be a valuable tool for interpreting observations. We also investigate some implications of efficient acceleration and the associated nonlinear effects on the modeling and interpretation of particle and photon observations of SNRs, and include a detailed study of the broad-band continuum emission

from the forward shock in SN1006.

Our basic model is given in Berezhko & Ellison (1999) where only protons are considered. Here, we extend the model to include electrons and alpha particles, and calculate the broad-band, continuum photon emission from the ion and electron distributions (Ellison & Berezhko 1999a). For protons, the injection process whereby some fraction of the shock heated plasma becomes accelerated to superthermal energies is, of necessity, parameterized but the model allows for the investigation of parameters against observations. Unfortunately, the theory of electron injection and acceleration in shocks is on a less secure footing than for protons, so we are forced to use additional parameters for electron injection. Helium is included without accounting for the enhancement effect known to occur for high mass to charge number ions (e.g., Baring et al. 1999), but this approximation has little effect on the results presented here.

We claim our nonlinear model, in spite of its approximations and parameters, is far more physically meaningful than the test-particle power laws that are still routinely assumed by many workers as the outcome from shock acceleration. A crucial property of efficient, nonlinear shock acceleration is the interconnection of the entire particle distribution from thermal to the highest energies, and the linkage between protons and electrons. Because energy is conserved, a change in the production efficiency of the highest energy cosmic rays *must* impact the thermal properties of the shock heated gas and vice versa. If more energy goes into relativistic particles, less is available to heat the gas. In contrast, the power laws assumed by test-particle models have no connection with the thermal gas, energy conservation does not constrain the normalization of the power law, and the spectral index can be changed with no feedback on the thermal plasma. The availability of an easy-to-use nonlinear shock acceleration model will have important implications for interpreting the broad-band emission from cosmic sources. In particular, the model presented here can efficiently explore parameter space to determine which quantities are the most dominant in controlling the spectral character and detectability of a remnant’s emission in each waveband. The density of the ambient interstellar medium and the environmental magnetic field strength are the most interesting and critical parameters in this regard. It is clear that adjusting parameters to fit one component, say radio, changes the predicted fluxes at all other frequencies and most significantly in the X-ray band. Based on constraints imposed by radio and γ -ray observations, the simple model can distinguish, as a function of source model and environmental parameters, the relative contributions of synchrotron (from TeV electrons) and non-thermal bremsstrahlung to the X-ray continuum. Our model predicts the shape of the full, nonthermal electron spectrum and, for sources where non-thermal bremsstrahlung is significant, X-ray line models may need to consider these non-thermal distributions.

Conversely, the model possesses the ability to predict TeV fluxes given detections at other energies. One of the most perplexing developments of cosmic ray physics is the lack of clear detections of pion-decay photons from SNRs. The original predictions of Drury, Aharonian, & Völk (1994) are well above current upper limits from EGRET and ground-based TeV telescopes. It is almost universally assumed that supernova blast waves accelerate cosmic ray ions at least up

to the “knee” near 10^{15} eV, and if so, these high energy ions will interact with the ambient gas and produce pions which will decay into GeV and TeV photons. The distinctive pion-decay bump was expected to be seen with current sensitivities and the lack of detection means there is still no direct evidence that SNRs produce cosmic ray ions and is something of a concern for both theorists and builders of γ -ray telescopes. Since the detectability depends on source parameters, observers critically need selection criteria which reliably predict which SNRs, observed at other frequencies, are likely to be bright at γ -ray energies. This is particularly true for ground-based air Čerenkov telescopes which must devote weeks or even months observing a single position in the sky to obtain good statistics. As we show in our survey below, the model can provide these selection criteria. For most of the cases we have studied, supernovæ which explode in low-density, low magnetic field regions have the largest TeV to radio flux ratios.

2. SIMPLE NONLINEAR SHOCK MODEL

The model of Berezhko & Ellison (1999) synthesizes the essential features of two complimentary approaches to nonlinear shock acceleration, namely the semi-analytical diffusion equation method of Berezhko et al. (1996) and others (e.g., Kang & Jones 1991, 1995) and the Monte Carlo technique of e.g., Ellison et al. (1996). The premise of the model of Berezhko & Ellison is that the main aspects of time-dependent, nonlinear shock acceleration can be understood in the framework of a plane-wave, steady-state assumption with simple approximations for the accelerated particle spectrum. An essential element of nonlinear acceleration is particle escape and Ellison & Berezhko (1999b) showed (and we confirm here) that the dynamic effects of particle escape are essentially the same in a plane-wave, steady-state shock as in an evolving, spherical shock. The two very different scenarios agree because the process of particle decoupling (i.e., escape) from shocks at high energies produces the same shock modification and increased compression ratio in the evolving, spherical shock solution, where particle ‘escape’ is mimicked by energy ‘dilution’ in the ever expanding upstream volume, as it does in the plane-wave approximation, where particles leave at a maximum cutoff energy or a free-escape-boundary (FEB). The essential point is that particle escape from strong shocks is a *fundamental part* of the nonlinear acceleration process and is determined primarily by energy and momentum conservation, not time-dependence or a particular geometry. The injection efficiency, together with the ‘shock size’ (however it may be determined), set the shock structure and determine the overall acceleration efficiency.

In other words, in a real, finite sized shock, geometry is important for determining the maximum value of momentum, p_{\max} , where the spectrum cuts off, and particle escape comes about naturally. In the plane-wave approximation, escape is parameterized with a FEB, but the model can still be used to good effect with this restriction. Similarly, since the majority of particles accelerated by an expanding SNR blast wave typically have acceleration times which are much shorter than the time scale of the system (in fact, even the highest energy particles expected in SNRs have acceleration times a few times shorter than the remnant age, e.g., Berezhko 1996), a steady-state

approximation can be used for modeling the particles accelerated by a strongly modified shock. We give a quantitative verification of this claim in Ellison & Berezhko (1999b), and demonstrate it below in detail for the SNR SN1006.

2.1. Protons

The non-linearity of the acceleration process in high Mach number shocks is manifested through the feedback of the ions on the spatial profile of the flow velocity (e.g., Drury 1983; Jones & Ellison 1991), which in turn determines the particle distribution. The accelerated population presses on the upstream plasma and slows it. An upstream precursor forms, in which the flow speed (in the absence of instabilities) is monotonically decreasing. The net effect that emerges is one where the overall compression ratio, r_{tot} , from far upstream to far downstream of the subshock discontinuity, exceeds that obtained in the test-particle scenario, while the subshock compression ratio, r_{sub} , which is mainly responsible for heating the gas, is less than the test-particle compression. This phenomenon was identified by Eichler (1984), and Ellison & Eichler (1984), and arises for two reasons. The most important is that particle escape from strong shocks drains energy and pressure which must be compensated for by ramping up the overall compression ratio to conserve the fluxes. The second reason is that relativistic particles, with their softer equation of state, contribute significantly to the total pressure making the shocked plasma more compressible. Since particle diffusion lengths are generally increasing functions of momentum (e.g., Giacalone et al. 1993; Scholer, Kucharek, & Giacalone 2000), high momentum particles sample a broader portion of the flow velocity profile, and hence experience larger compression ratios than low momentum particles. Consequently, higher momentum particles have a flatter power-law index than those at lower momenta, thereby dominating the pressure in a nonlinear fashion and producing a concave upward spectral curvature which is the trademark of nonlinear shock acceleration.

It is precisely this spectral concavity that can be compactly approximated by the simple model of Berezhko & Ellison (1999). Berezhko & Ellison assume that the accelerated part of the shocked particle phase-space distribution, $f(p)$, above a superthermal injection momentum, p_{inj} , can be described as a three-component power law:

$$f(p) = \begin{cases} a_{\text{inj}} (p/p_{\text{inj}})^{-q_{\text{sub}}} & \text{if } p_{\text{inj}} \leq p \leq m_{\text{p}} c , \\ a_{\text{mc}} [p/(m_{\text{p}} c)]^{-q_{\text{int}}} & \text{if } m_{\text{p}} c \leq p \leq p_{01} , \\ a_{\text{max}} (p/p_{01})^{-q_{\text{min}}} & \text{if } p_{01} \leq p \leq p_{\text{max}} . \end{cases} \quad (1)$$

Here, q_{sub} is determined by the subshock compression ratio i.e.,

$$q_{\text{sub}} = 3r_{\text{sub}}/(r_{\text{sub}} - 1) , \quad (2)$$

q_{min} is given by,

$$q_{\text{min}} = 3.5 + \frac{3.5 - 0.5 r_{\text{sub}}}{2r_{\text{tot}} - r_{\text{sub}} - 1} , \quad (3)$$

(see Berezhko 1996 for a full discussion of this equation and Malkov 1997, 1999 for an alternative derivation) and

$$q_{\text{int}} = (q'_{\text{tp}} + q_{\text{min}})/2, \quad (4)$$

where the prime indicates that we use

$$r'_{\text{tot}} = \frac{(\gamma_{2g} + 1)M_{\text{S}0}^2}{(\gamma_{2g} - 1)M_{\text{S}0}^2 + 2} \leq 4 \quad (5)$$

to calculate q'_{tp} . The far upstream sonic Mach number is $M_{\text{S}0}$, $\gamma_{2g} = 5/3$ is the adiabatic index of the shocked gas excluding cosmic rays, and the normalization factors are $a_{\text{mc}} = a_{\text{inj}} [p_{\text{inj}}/(m_p c)]^{q_{\text{sub}}}$, and $a_{\text{max}} = a_{\text{mc}} (m_p c/p_{01})^{q_{\text{int}}}$. The full explanation of these terms (including the normalization a_{inj} in terms of input parameters) is given in Berezhko & Ellison (1999), but for here it is only necessary to state that the nonlinear spectrum can be determined with four arbitrary parameters: (1) p_{inj} , (2) the rate of proton injection, $\eta_{\text{inj,p}}$, (3) the maximum momentum, p_{max} , where the spectrum cuts off, and (4) p_{01} . The results are relatively insensitive to p_{01} which we take as $p_{01} = 0.01p_{\text{max}}$ if $p_{01} > m_p c$ or $p_{01} = m_p c$ otherwise, and p_{inj} and $\eta_{\text{inj,p}}$ are related, leaving essentially two free parameters to describe the proton spectrum (here and elsewhere, m_p is the proton rest mass). In this steady-state description, the proton injection *rate*, $\eta_{\text{inj,p}}$ (Berezhko et al. use the notation η), is equivalent to the fraction of total shocked proton number density, n_2 , in protons with momentum $p \geq p_{\text{inj}}$. The scheme we adopt for determining the scale length that fixes p_{max} is described in Section 3.1.

The thermal portion of the downstream spectrum is taken to be a Maxwell-Boltzmann distribution at the shocked temperature and density, i.e., $T_2 = P_2 m_p / (\rho_2 k)$, where the downstream pressure, P_2 , and downstream density, $\rho_2 = \rho_0 r_{\text{tot}}$, are determined by the solution, i.e., they couple to the shock dynamics. No extra parameters are required to specify the thermal portion of the proton distribution other than to assume it is Maxwell-Boltzmann. In Figure 1 (Fig. 5 from Berezhko & Ellison 1999), we compare results from the simple model with those of a Monte Carlo shock simulation used as a reference. The Monte Carlo simulation calculates the entire spectrum from thermal energies upward and has an internally consistent determination of the injection efficiency. Using this value of $\eta_{\text{inj,p}}$ in the simple model (the solid triangle is at p_{inj}) gives an excellent match between the two techniques. The extremely high compression ratios occur because only adiabatic heating of the shock precursor is assumed. When Alfvén wave heating is included (as it is in all of the results presented below except those shown in Figure 2), considerably smaller r_{tot} 's result (see Berezhko & Ellison 1999 for a discussion of Alfvén wave heating).²

²Helium is included in the calculation of Eqs. (1) in an approximate way by adding a pressure contribution equal to $n_{\text{He}}/n_{\text{H}}$ times the energetic proton pressure. This neglects any enhancement effects for heavy ions, but these could be incorporated in the simple model with a parameterization such as used by Berezhko & Ksenofontov (1999). Based on the work of Baring et al. (1999), we expect the contribution of helium to the pion-decay emission to be no more than 50% of the proton contribution.

2.2. Electrons

Before describing how electrons are treated in our simple model, we note that electron injection is harder to characterize than proton injection for several fundamental reasons. One stems from the basic point that the shock structure is determined almost totally by the ions, since they carry most of the momentum, so general considerations of momentum and energy conservation constrain their behavior. Internally-consistent models of ion injection can be developed without a detailed knowledge of the complex plasma processes, and these models have been shown to match spacecraft observations of ion acceleration at heliospheric shocks (e.g., Ellison, Möbius, & Paschmann 1990; Baring et al. 1997) and hybrid simulations (e.g., Giacalone et al. 1997). Electrons, on the other hand, carry little momentum and don't influence the shock structure substantially so they act basically as test particles. Because of this, their injection and acceleration efficiencies (at nonrelativistic energies at least) are sensitive to the details of the complex wave-particle plasma interactions, which are not well understood. Furthermore, since protons determine the overall shock dynamics, plasma simulations wishing to describe electrons self-consistently must include protons self-consistently as well, forcing prohibitively large ranges in time and length scales. Compounding the problem, spacecraft observations of heliospheric shocks have not until very recently (i.e., Terasawa et al. 1999) detected the injection and acceleration of *thermal* electrons. This, in contrast to the many observations of thermal proton injection and acceleration, has made it impossible to infer the properties of electron injection and acceleration from in situ observations, or even, until recently, confirm that diffusive shock acceleration of electrons from the thermal background takes place.

In order to include electrons in the simple model we note that particles with the same upstream diffusion length, κ/u_0 (κ is the diffusion coefficient and u_0 is the far upstream shock speed),³ have the same acceleration rate. That is, electrons and protons will obtain the same spectral shape if they have the same diffusion coefficient $\kappa_e(p) = \kappa_p(p)$ in a considered momentum range. Since the diffusion coefficient $\kappa = \lambda(R)v/3$ depends not only on the particle rigidity, R , but also on their speed, v , which is different for electrons and protons at $p < 1$ GeV/ c , one might conclude that, in general, the shapes of the accelerated electron and proton spectra are different. However, it is easy to show that the electron and proton spectral shapes should, in fact, be very similar at superthermal energies. At relativistic energies, $E \gg m_p c^2$, the interaction with the magnetic field of electrons and protons of the same gyroradius (or rigidity) is indistinguishable if we assume any effects from helicity are insignificant. Therefore, the shape of the electron spectrum, $f_e(p)$, at $p \gg m_p c$ is the same as the proton spectrum, $f_p(p)$. Furthermore, to the accuracy of the simple proton model, where we assume that protons with $p \geq m_p c$ have speed c , and those with $p < m_p c$ have speed $v = p/m_p$, the spectral shapes will be the same for all $p \geq m_p c$. To the same accuracy, electrons with momenta $p < m_p c$ have smaller diffusion lengths than protons at $p = m_p c$ and they 'feel' only part of the shock transition, i.e., the subshock as assumed in the simple model. Therefore, just as we assume for the protons, the spectrum of accelerated electrons at $p < m_p c$ can be approximated

³Everywhere, the subscript '0' implies far upstream values and the subscript '2' implies far downstream values.

by the power law $f_e \propto p^{-q_{\text{sub}}}$, independent of the diffusion coefficient $\kappa_e(p)$, as long as κ is an increasing function of momentum.

Thus within the accuracy of the simple model,

$$f_e(p) = K_{ep} f_p(p), \quad (6)$$

at all superthermal energies, where the value of the numerical factor, K_{ep} , is determined by the relation between the electron and proton injection rates, i.e., using Eq. (1) we have $K_{ep} = (a_{\text{inj},e}/a_{\text{inj},p}) [p_{\text{inj},e}/p_{\text{inj},p}]^{q_{\text{sub}}}$, where the subscripts e and p denote electrons and protons, respectively. Unfortunately there are no reliable theoretical predictions for this relation so we parameterize it. We remark that if the damping of high frequency waves near thermal energies is strong enough to inhibit electron scattering, there will exist a range of suprathemal electron momenta where the electron diffusion coefficient and length are larger than the proton ones, i.e., $\kappa_e > \kappa_p$ (e.g., Levinson 1992, 1994). This case is considered in Baring et al. (1999), where the inefficient scattering of electrons causes their diffusion lengths to lengthen and *increases* their steady-state injection efficiencies. If this is the case, the electron spectra in the sub-GeV range may be quite different from those shown here and these differences can be particularly relevant to radio synchrotron and nonthermal bremsstrahlung emission.

If we make the specific assumption that the scattering mean free path is

$$\lambda = \eta_{\text{mfp}} r_{g,\text{max}} (r_g/r_{g,\text{max}})^\alpha, \quad (7)$$

where η_{mfp} is a parameter independent of particle momentum (Baring et al. 1999, use the notation η), $r_g = p/(qB)$ is the gyroradius in SI units, $r_{g,\text{max}}$ is the gyroradius at the maximum momentum, p_{max} , and α is a constant parameter ($\alpha = 1 = \eta_{\text{mfp}}$ is roughly the Bohm limit), then electrons and protons which satisfy,

$$\eta_{\text{mfp},e} p_e^\alpha v_e = \eta_{\text{mfp},p} p_p^\alpha v_p, \quad (8)$$

obtain the same spectral shape. Since we obtain the proton spectrum from the simple model, and if we assume that η_{mfp} is the same for electrons and protons, Eq. (8) allows us to determine the electron spectrum by finding the momenta dividing the three-component power law, i.e., the intervals where q_{sub} , q_{int} , and q_{min} in Eq. (1) apply. We note that the above is just for concreteness and that, within the approximations of our simple model, Eq. (6) holds and we do not have to make any specific assumptions concerning the form of the particle diffusion coefficient other than that it is a monotonically increasing function of momentum.

In the top panel of Figure 2 we show examples of $f_e(p)$ (dashed and dotted curves) and $f_p(p)$ (solid curve) obtained assuming Eq. (7) with $\alpha = 1$. As just explained, electrons and protons have identical superthermal shapes apart from a slight offset near $m_p c$ caused by assuming Eq. (8) rather than Eq. (6).

To set the amplitude of the superthermal electron spectrum, we find it convenient to use the electron to proton density ratio at relativistic energies, $(e/p)_{\text{rel}}$. We chose $(e/p)_{\text{rel}}$, rather than

some injection parameter, $\eta_{\text{inj},e}$, analogous to $\eta_{\text{inj},p}$, since $(e/p)_{\text{rel}}$ can be constrained by observations such as those of Galactic cosmic rays, which suggest values around 1–5% (e.g., Müller & Tang 1987; Müller et al. 1995) in the 1–10 GeV range. The final parameter needed to completely specify the electron spectrum is the shocked electron to proton temperature ratio, T_{e2}/T_{p2} , for which there is considerable latitude given uncertainties in the shock speed and other parameters for individual SNRs that leaves T_{p2} ill-determined observationally. Note that detections of X-ray emission (e.g., Zimmermann, Trümper, & Yorke 1996) can constrain T_{e2} if contributions from nonthermal electron components can be ruled out. Given T_{e2}/T_{p2} and $(e/p)_{\text{rel}}$, it is straightforward to compute $\eta_{\text{inj},e}$, as follows. The number density of particles per unit energy interval, dN/dE , is given by,

$$\frac{dN}{dE} = 4\pi p^2 f(p) \frac{dp}{dE}, \quad (9)$$

where $dp/dE = (E + m_0 c^2)/(p c^2)$, for $m_0 = m_e, m_p$ as the case may be. Here and elsewhere, E is the kinetic energy. Exploiting the fact that the electron and proton phase space distributions have essentially the same shape we can write the ratio at a given nonrelativistic energy, $E_e = E_p = E_{\text{NR}} \ll m_e c^2$,

$$\frac{\eta_{\text{inj},e}}{\eta_{\text{inj},p}} \equiv \frac{(dN/dE)_e}{(dN/dE)_p} \Big|_{E_{\text{NR}}} = \frac{a_{\text{inj},e} m_e p_e (p_e/p_{\text{inj},e})^{-q_{\text{sub}}}}{a_{\text{inj},p} m_p p_p (p_p/p_{\text{inj},p})^{-q_{\text{sub}}}} = \frac{a_{\text{inj},e}}{a_{\text{inj},p}} \left(\frac{m_e}{m_p}\right)^{3/2} \left(\frac{T_{e2}}{T_{p2}}\right)^{q_{\text{sub}}/2}, \quad (10)$$

since $p_{\text{inj},e} \propto (m_e T_{e2})^{1/2}$, $p_e \propto (m_e E_e)^{1/2}$ and likewise for protons. This can be inverted to yield $a_{\text{inj},e}/a_{\text{inj},p}$. At identical relativistic energies, $E_e = E_p = E_{\text{rel}} \gg m_p c^2$, since p_{01} is identical for protons and electrons, we have,

$$(e/p)_{\text{rel}} \equiv \frac{(dN/dE)_e}{(dN/dE)_p} \Big|_{E_{\text{rel}}} = \frac{p_e^2 a_{\text{max},e} (p_p/p_{01})^{-q_{\text{min}}}}{p_p^2 a_{\text{max},p} (p_e/p_{01})^{-q_{\text{min}}}} = \frac{a_{\text{max},e}}{a_{\text{max},p}} = \frac{a_{\text{inj},e}}{a_{\text{inj},p}} \left(\frac{m_e}{m_p} \frac{T_{e2}}{T_{p2}}\right)^{q_{\text{sub}}/2}, \quad (11)$$

since $p_p = p_e$ at relativistic energies. The last equality is obtained using the definition of a_{max} given just after Eq. (5). Eqs. (10) and (11) define the relationship between $\eta_{\text{inj},e}$, T_{e2}/T_{p2} , and $(e/p)_{\text{rel}}$, with the explicit dependence on T_{e2}/T_{p2} disappearing when $a_{\text{inj},e}$ is specified.

Comparison of Eqs. (10) and (11) shows that the number density ratio decreases by a factor of $(m_e/m_p)^{(q_{\text{sub}}-3)/2}$ in going from fully nonrelativistic to fully relativistic energies. For strong shocks, $r_{\text{sub}} \sim 3$ and $q_{\text{sub}} \sim 4.5$, so producing an electron to proton ratio of $(e/p)_{\text{rel}} \sim 0.01$ at relativistic energies, as observed for galactic CRs, implies that the electron injection rate at nonrelativistic energies must be approximately equal to the proton rate, i.e., $\eta_{\text{inj},e} \simeq \eta_{\text{inj},p}$. This conclusion holds whether the thermal electrons and protons are in equipartition or not. However, it is highly likely that the injection energy scales strongly with the shocked temperature, implying that $T_{e2} \sim T_{p2}$, i.e., it is unlikely that $(e/p)_{\text{rel}} \sim 0.01$ can be obtained unless the shocked electron and proton temperatures are nearly equal,⁴ a result suggested by some thermal X-ray signatures of SNRs (e.g., Zimmermann, Trümper, & Yorke 1996).

⁴The work presented here implicitly assumes that all of the accelerated protons and electrons originate from the

For the example shown in Figure 2, we have chosen $T_{e2}/T_{p2} = 1$, and used $(e/p)_{\text{rel}} = 0.05$ (dashed line) and $(e/p)_{\text{rel}} = 0.01$ (dotted line). The spectra also include an exponential cutoff (not included in the initial Berezhko & Ellison 1999 work) so that $f(p)$ given by Eqs. (1) becomes (see Berezhko & Krymsky 1996 and Berezhko et al. 1996):

$$f(p) \rightarrow f(p) \exp \left[-\frac{1}{\alpha} \left(\frac{p}{p_{\text{max}}} \right)^\alpha \right], \quad (12)$$

where the α is the same as in Eqn. (7).

The bottom panel of Figure 2 shows the differential flux, $dJ/dE = [v/(4\pi)]dN/dE$, in particles per cm^2 per sec per ster per MeV. For $(e/p)_{\text{rel}} = 0.05$, $\eta_{\text{inj},e} = 0.012$, while for $(e/p)_{\text{rel}} = 0.01$, $\eta_{\text{inj},e} = 2.5 \times 10^{-3}$, if we assume that the electron and proton injection energies are the same.

Finally, we define the acceleration efficiency, ϵ_{rel} , as the fraction of total incoming energy flux that goes into particles with momentum $p \geq m_p c$, i.e.,

$$\epsilon_{\text{rel}} = \frac{[\gamma_2/(\gamma_2 - 1)] P_{\text{rel},2}(> m_p c) u_2 + F_E}{(1/2)\rho_0 u_0^3 + (5/2) P_0 u_0}, \quad (13)$$

where $P_{\text{rel},2}(> m_p c)$ is the downstream pressure in particles of momentum $m_p c$ or greater, u is the bulk flow speed in the shock frame, γ_2 is the effective downstream ratio of specific heats including the effects of relativistic particle pressure, and we have taken the ratio of specific heats for the unshocked plasma to be $5/3$. The escaping energy flux, F_E , is included in this definition since these are accelerated particles that only leave the system after obtaining an energy $E \sim E_{\text{max}}$. The efficiency for selected examples are listed in Tables 1 and 2 under ‘Output values’.

2.3. Photons

The photon emission processes considered in this paper are those discussed at length in Baring et al. (1999): synchrotron emission that pertains to the radio to X-ray wavebands, inverse Compton scattering of cosmic microwave background radiation that contributes to the gamma-ray signal, X-ray/gamma-ray bremsstrahlung emission of thermal and energetic electrons interacting with both ambient electrons and protons,⁵ and pion decay gamma-rays spawned by p - p collisions involving the accelerated cosmic rays. As in Baring et al. (1999), we explicitly include the photon production

thermal background. In fact, superthermal seed populations exist, such as the Galactic cosmic rays and, in young SNRs, positrons and electrons from radioactive decay of freshly synthesized material will be accelerated if they encounter local shocks. For simplicity, however, we assume that the contributions from these sources to the freshly accelerated thermal material is small, noting that the ambient ISM density exceeds that of cosmic rays by several orders of magnitude.

⁵We note that, to correct some typographical errors and improve the accuracy of an approximation to the e - e bremsstrahlung cross-section, Eqs. (A2) and (A4) in Baring et al. (1999) should be modified such that all γ_e ’s in

from He–p and He–He collisions. While Sturmer et al. (1997) were the first to examine the radiative signatures of all of these components, Baring et al. (1999) were the first to treat them all in the context of a detailed model of nonlinear shock acceleration. Generally, infrared radiation fields peculiar to individual remnants contribute only a minority of the inverse Compton signal (e.g., Gaisser, Protheroe, & Stanev 1998; but see de Jager & Mastichiadis’ 1997 discussion of the environment of W44). To date, and also in this paper, synchrotron self-Compton contributions are neglected, being important only in strongly magnetized (i.e., $B \gtrsim 100\mu\text{G}$) remnants such as Cas A. Furthermore, inverse bremsstrahlung from fast ions contributes insignificantly in general (Baring, Jones, & Ellison 2000), and is accordingly neglected here.

Losses from synchrotron and inverse-Compton emission are included and combined such that electron spectra cutoff at an energy

$$E_{\text{max}} \simeq 1.6 \times 10^5 \eta_{\text{mfp}}^{-1/2} \left(1 - \frac{1}{r_{\text{tot}}}\right)^{1/2} \left(\frac{V_{\text{sk}}}{\text{m/s}}\right) \times \left[\left(\frac{B_0}{\text{G}}\right)^{-1} + r_{\text{tot}} \left(\frac{B_2}{\text{G}}\right)^{-1}\right]^{-1/2} \left[\left(\frac{B_2}{\text{G}}\right)^2 + \left(\frac{B_{\text{cbr}}}{\text{G}}\right)^2\right]^{-1/2} \text{ eV}, \quad (15)$$

where V_{sk} is the shock speed and $B_{\text{cbr}} = 3.23 \mu\text{G}$ is the equivalent magnetic field of the cosmic background radiation and accounts for inverse-Compton losses. This expression differs slightly from that in Baring et al. because we explicitly allow for the downstream field B_2 to be different from B_0 . Also, in order to be consistent with the work of Berezhko, Ksenofontov, & Petukhov(1999a), we take the perpendicular component of the downstream magnetic field to the line of sight to be $B_{2\perp} = 0.5B_2$ in calculating the synchrotron emission.

3. MODELING SNR PHOTON EMISSION

Instead of arbitrarily choosing the shock speed and maximum acceleration energy, we use a model of SNR evolution by Truelove & McKee (1999) that continuously maps between the free expansion and Sedov phases to give the shock parameters as a function of explosion energy, E_{sn} , ejecta mass, M_{ej} , and remnant age, t_{snr} . For this work, we only consider uniform distributions for the ambient ISM mass, appropriate to Type Ia progenitors. We do allow for a power-law density profile for the ejecta, as in Chevalier (1982), i.e.,

$$\rho \propto t_{\text{snr}}^{-3} (r/t_{\text{snr}})^{-n}, \quad (16)$$

Eq. (A2) are replaced by $\gamma_e - 1$, and Eq. (A4) there is written as

$$A(\varepsilon_\gamma, \gamma_e) = 1 - \frac{10}{3} \frac{(\gamma_e - 1)^{1/5}}{\gamma_e + 1} \left(\frac{\varepsilon_\gamma}{\gamma_e}\right)^{1/3} \quad (14)$$

for ε_γ where $A(\varepsilon_\gamma, \gamma_e)$ is positive; otherwise $A(\varepsilon_\gamma, \gamma_e)$ is set to zero.

where ρ is density, r is radius, and n is a constant, but only consider the forward shock. Examples with forward and reverse shocks are given in Ellison (2000). We caution that care must be used in applying our acceleration model and associated predictions of broad-band emission to Type II supernovæ, which may explode in environments that are far from uniform, being strongly modified by the stellar wind generated by their massive progenitors.

In Figure 3a we show the *instantaneous* particle spectra produced by the forward shocks in two examples which differ widely in ambient parameters. We have a high density, high ejecta mass, high B -field example (‘H’ with heavy-weight curves) with proton number density $n_{p0} = 10 \text{ cm}^{-3}$, $M_{\text{ej}} = 5M_{\odot}$, and $B_0 = 30 \times 10^{-6} \text{ G}$ (more typical of Type II SNæ), and a low density, low ejecta mass, low B -field example (‘L’ with light-weight curves) with $n_{p0} = 0.01 \text{ cm}^{-3}$, $M_{\text{ej}} = 1M_{\odot}$, and $B_0 = 3 \times 10^{-6} \text{ G}$ (more typical of Type Ia SNæ). A full listing of the parameters is given in Table 1 under columns marked ‘High’ and ‘Low’ but all other input parameters are the same between these two models, namely: $E_{\text{sn}} = 10^{51} \text{ erg}$, $t_{\text{snr}} = 1000 \text{ yr}$, $T_{e2}/T_{p2} = 1$, $(e/p)_{\text{rel}} = 0.03$, and $\eta_{\text{inj,p}} = 1 \times 10^{-3}$. Figure 3b shows photon fluxes at the Earth assuming a distance, $D_{\text{snr}} = 1 \text{ kpc}$ and an emission volume, $V_{\text{emis}} = 1 \text{ pc}^3$. All output parameters are given in Table 1. In all of the examples in this paper we assume the plasma is fully ionized and the ambient helium number density to be $0.1 n_{p0}$. We further assume that the unshocked helium temperature *per nucleon* equals the proton temperature, T_{p0} (this is typically observed in the heliosphere), and that the unshocked electron temperature equals T_{p0} .

There are some striking differences between the photon spectra for these parameter sets which represent a reasonable spread for various types of SNRs. First, the three order of magnitude difference in n_{p0} and one order difference in B_0 produce much stronger emission, per unit emission volume, for the high values. Next, for high values, the TeV emission is dominated by pion-decay with inverse-Compton being completely insignificant (and not shown in Figure 3b), while for low values, the TeV emission is dominated by inverse-Compton. The inverse-Compton from the low value example also yields the highest photon energies. At hard X-ray energies (10-100 keV), the emission from the high density example has a strong nonthermal bremsstrahlung component, while for the low density example, the X-rays $< 100 \text{ keV}$ are almost totally from synchrotron emission from high energy electrons. Deducing the shifting dominance of the various emission processes as parameters vary is an important goal of this work.

3.1. Parameter Survey

As indicated by the previous examples, nonlinear shock acceleration is complicated and the solutions we describe have a large number of parameters, even in the homogeneous environment we assume. The input parameters are: E_{sn} , M_{ej} , t_{snr} , n_{p0} , B_0 , n , D_{snr} , and V_{emis} . Added to these are the parameters intrinsic to the model: $\eta_{\text{mf,p}}$, $\eta_{\text{inj,p}}$, T_{e2}/T_{p2} , and $(e/p)_{\text{rel}}$, plus what we call ‘general model’ assumptions. These include α , p_{01} , equation (12), and the assumptions of ambient and ejecta mass distributions. The maximum momenta where the spectra cut off are also model

parameters, but they are determined from the SNR model (η_{mfp} becomes important here) as was described in Baring et al. (1999). That is, in determining the maximum momenta of protons, we first assume equation (7) and then set the diffusive shock acceleration time, t_{acc} , equal to t_{snr} , or set the upstream diffusion length equal to 1/4 of the shock radius, whichever produces the lowest p_{max} .⁶ For electrons, p_{max} is equal to that of the protons or to the value determined from combined synchrotron and inverse-Compton losses (see Baring et al. 1999, for details), whichever is less.

3.1.1. Emission volume

For a uniform environment, we can estimate the emission volume in the following way. The contact discontinuity separates the swept up ISM material from the ejecta and acts as the piston for the forward shock. During the free expansion and early Sedov phases, the swept up material forms a nearly uniform, dense shell behind the forward shock such that,

$$R_{\text{sk}}^3 \rho_0 \approx \rho_{\text{shell}} (R_{\text{sk}}^3 - R_{\text{piston}}^3) , \quad (17)$$

where R_{piston} is the radius of the contact discontinuity, ρ_0 is the density of the background ISM, and ρ_{shell} is the density in the shell. In the approximation that the shell has uniform density, $\rho_{\text{shell}} = r_{\text{tot}} \rho_0$, i.e., it has the shocked density, ρ_2 . For large compression ratios, the thickness of the shell, $L = R_{\text{sk}} - R_{\text{piston}} \ll R_{\text{sk}}$, and we can write,

$$\frac{1}{r_{\text{tot}}} = 1 - \left(\frac{R_{\text{piston}}}{R_{\text{sk}}} \right)^3 = 1 - \left(\frac{R_{\text{sk}} - L}{R_{\text{sk}}} \right)^3 \approx \frac{3L}{R_{\text{sk}}} . \quad (18)$$

During later phases, the contact discontinuity will be far from the forward shock but we can then interpret L as the thickness of the dense shell behind the forward shock where most of the emission occurs independent of the position of the contact discontinuity. With these approximations, the emission volume can be estimated as

$$V_{\text{emis}} \approx (4\pi/3) R_{\text{sk}}^3 / r_{\text{tot}} , \quad (19)$$

so that the emission volume generally is considerably less than the total remnant volume.

3.1.2. Trends and Key Parameters

In Figures 4, 5, and 6 we plot the total photon emission varying a single parameter as indicated. All of these results are normalized to $D_{\text{snr}} = 1$ kpc and V_{emis} as given in Eqn. (19). Varying $\eta_{\text{inj,p}}$,

⁶In determining p_{max} at time t_{snr} , we make the approximation that the shock speed is constant at the value it has at t_{snr} . In fact, an accurate determination of p_{max} in an evolving remnant requires a more complete model than we use here, i.e., Berezhko (1996), which keeps track of the history of particles, adiabatic losses, and the numbers of particles accelerated at a given epoch. Despite this, our values will not differ by large factors from more realistic ones.

T_{e2}/T_{p2} , or $(e/p)_{\text{rel}}$ (Fig 4) produces relatively modest changes in the photon emission, particularly in the radio to X-ray and gamma-ray bands. An exception occurs for $\eta_{\text{inj,p}} = 10^{-5}$ (solid curve, Fig. 4a). This injection rate is low enough that a *test-particle* result occurs even though the Mach number is quite high ($M_{S0} \simeq 130$), i.e., the energy placed in superthermal particles is not enough to smooth the shock. A test-particle solution is different in two main ways from the nonlinear cases: the overall compression ratio, r_{tot} , is approximately four which is considerably less than for the higher injection rate cases, producing the steeper spectrum at the highest energies, and the shocked temperature is considerably higher than the nonlinear temperatures (as indicated by the position of the UV/X-ray thermal bremsstrahlung peak in panel 4a). While the gamma-ray flux drops in the test-particle regime, the concurrence of curves for higher $\eta_{\text{inj,p}}$ underlines the regulatory effect (e.g., Eichler 1984; Ellison & Eichler 1984; see also the review of Jones and Ellison 1991) of nonlinear acceleration.

Figure 4b reveals that by itself, the value of the parameter T_{e2}/T_{p2} is of little significance. This is because of its coupling to $\eta_{\text{inj,p}}$, and $(e/p)_{\text{rel}}$, as described in Section 2.2, so that by fixing $\eta_{\text{inj,p}}$, and $(e/p)_{\text{rel}}$, the non-thermal X-ray/soft gamma-ray bremsstrahlung flux and the hard gamma-ray pion decay and inverse Compton contributions remain approximately fixed. The proton temperature is determined by the shock dynamics solution.

Changes in the electron to proton ratio at relativistic energies, $(e/p)_{\text{rel}}$ (Fig. 4c), also produce important effects in the superthermal bremsstrahlung range, since this component depends on the normalization of the non-thermal electron distribution. As $(e/p)_{\text{rel}}$ increases, the super-GeV gamma-ray band shifts from being pion-decay dominated to having nearly equal bremsstrahlung, inverse-Compton, and pion-decay components. We show below examples with a more tenuous ISM where inverse-Compton dominates the gamma-rays so that the flux in this energy range becomes quite sensitive to the choice of $(e/p)_{\text{rel}}$.

The ambient density is expected to have a large natural range (Fig. 5a) and strongly influences the emitted flux. Low values of n_{p0} give the highest maximum energy with the $>\text{TeV}$ flux dominated by inverse-Compton. As n_{p0} increases, the pion-decay component becomes more pronounced in the 100 MeV to TeV range and bremsstrahlung becomes dominant in the X-ray band. X-ray emission is dominated by synchrotron at low n_{p0} , and the radio emission is relatively insensitive to n_{p0} with a slight flattening occurring at higher densities. Naively, one expects that the synchrotron and inverse Compton components should scale linearly with density increases, while the bremsstrahlung and pion decay contributions should be proportional to n_{p0}^2 . However, the global spectral properties are an accumulation of effects caused by the complexity of the nonlinear acceleration mechanism and the evolution of the SNR as given by the Truelove & McKee parameterization. As n_{p0} rises, the expanding supernova sweeps up its ejecta mass sooner, and therefore decelerates on shorter timescales, thereby reducing both the radius and volume of a remnant of given age, and lowering the shock speed, the compression ratio, and the downstream proton temperature T_{p2} [e.g., see Eq. (7) of Baring et al. 1999; and Table 2]. The bottom line is that the normalization of the overall distribution and the relative contributions of the various components, are not simple functions of

density and can vary strongly in narrow energy bands. The full set of parameters for Figure 5 is given in Table 2.

Some remarkable features in Figure 5a (where $B = 3\mu\text{G}$ for all four examples) include (i) for $n_{p0} > 1\text{ cm}^{-3}$ (i.e., the dotted curve, see also Figure 3), the radio to optical/UV emission is of thermal bremsstrahlung rather than synchrotron origin, (ii) the highest energy emission occurs for the lowest n_{p0} and is dominated by inverse-Compton, and (iii) the spectral shape in the X-ray band (1-100 keV) is highly sensitive to the density (thereby providing powerful observational diagnostics) and can have a strong nonthermal bremsstrahlung component at high n_{p0} .

Variations caused by adjusting the ambient magnetic field are illustrated in Fig. 5b (where $n_{p0} = 1\text{ cm}^{-3}$ for all four examples). The principal property immediately apparent is the anti-correlation between radio and GeV-TeV fluxes. The higher the value of B_0 , the brighter the radio synchrotron [scaling as $\sim B^{3/2}$; e.g., see Eq. (6.36) of Rybicki & Lightman 1979], which is the effect usually incorporated in test-particle SNR models (e.g. Mastichiadis & de Jager 1996). In addition, however, the hard gamma-ray emission becomes fainter with increasing B_0 . This property arises mostly because of the influence of the magnetic field on the shock dynamics and total compression ratio. The Alfvénic Mach number drops and Alfvén wave heating in the precursor becomes stronger as B_0 increases causing r_{tot} to decrease. This weakening of the shock steepens the particle distributions and the overall photon spectrum, with the net effect of a reduction of the gamma-ray flux together with a change in its spectral index.⁷ The emission from radio through the X-ray band is dominated by synchrotron emission from energetic electrons for $B_0 > 10\ \mu\text{G}$, with bremsstrahlung dominating X-rays for $B_0 \leq 3\ \mu\text{G}$. Another consequence of a rise in B_0 is that the maximum *ion* energy increases while the maximum *electron* energy declines due to synchrotron losses. This causes pion-decay to dominate the gamma-ray band and the UV/soft X-ray synchrotron peak becomes approximately independent of B_0 , a well-known property (e.g., de Jager et al. 1996; Reynolds 1996) of cooling-limited synchrotron radiation. Note again that we omit the regime $B_0 > 100\mu\text{G}$ where the Alfvénic Mach number is as low as a few and where second-order Fermi acceleration is important (see Bykov et al. 2000 and references therein), an effect beyond the scope of the present work.

The plots in Fig. 5 include the approximate integral flux sensitivities (adjusted for the E_γ^2 times differential flux representation) of the proposed Veritas experiment (Weekes et al. 1999) and the planned GLAST mission (Gehrels & Michelson 1999). These represent the probability that each of these experiments will detect photons above a given energy, and clearly indicate that GLAST and Veritas will make significant observational progress in the 100 MeV–100 GeV and 100 GeV–10 TeV bands, if SNRs emit according to the predictions here. CELESTE provides somewhat better sensitivity in the limited 50-70 GeV range, but we chose the Veritas sensitivity as a benchmark for

⁷The spectrum is further steepened because the Alfvén waves which do the scattering are assumed to move through the upstream plasma such that they move with the Alfvén speed away from the shock when viewed from the local plasma frame.

atmospheric Čerenkov telescopes (ACTs). Several new TeV programs are in the works, including MAGIC (Lorenz 1997) in the Canary islands, and HESS (e.g. Kohnle et al. 1999) and CANGAROO-III in the southern hemisphere; their sensitivities differ only modestly in energy range and flux from the ones depicted for Veritas. Because of the “saturation” of gamma-ray spectra at low densities, due to the insensitivity of inverse Compton emission to ISM density, for reasonable ISM fields these experiments should have no difficulty detecting remnants throughout the Sedov epoch and prior to the radiative phase. The only way this cannot materialize is for shocks at remnant shells not to be efficiently accelerating particles to energies beyond around 10 GeV, i.e., contrary to general expectations. Therefore, we anticipate positive detections in a number of SNRs in and out of the galactic plane, and even the most pessimistic case of no detections will lead to an improved understanding of particle acceleration.

In particular, remnants in moderately dense environs (i.e. $\gtrsim 1 \text{ cm}^{-3}$) will be ideal candidates for GLAST to search for the π^0 bump emission so clearly evident in the higher density cases in Fig. 5a. A clearer indication of this can be found in Baring (2000), where these model spectra are compared with the simulated *differential* flux sensitivity expected for GLAST, a truer indicator of the ability of the instrument to perform spectral measurements; Baring (2000) observes that the π^0 bump will be a clearly discernible spectral structure when ISM densities exceed around 0.3 cm^{-3} . Confirmation of the existence of accelerated ions that spawn such a gamma-ray signature is an unambiguous signature of cosmic ray production. We note that the EGRET sensitivity over the 100 MeV – 10 GeV band is in the 10^{-5} – $10^{-4} \text{ MeV cm}^{-2} \text{ sec}^{-1}$ range, so that only remnants with ambient densities exceeding around 0.3 cm^{-3} would be possibly detectable by EGRET. Moreover, EGRET would only be sensitive to pion decay bumps when the environmental densities are quite large, well above 10 cm^{-3} .

In Fig. 6 we show variations in the SN explosion energy and the age of the remnant. Adjusting E_{sn} clearly produces little change in the broad-band spectral shape, merely modifying the normalization due to changes in the radius and volume of the remnant. On the other hand, at early times (i.e., $t_{\text{snr}} \lesssim 300 \text{ yr}$), the SNR age has a strong effect on the flux, mainly because the remnant volume is small prior to the Sedov phase. During these early times, which consists mostly of the free expansion phase, the shock is extremely nonlinear in nature, obtaining a very large compression ratio ($r_{\text{tot}} \simeq 25$ when $t_{\text{snr}} = 30 \text{ yr}$ and $r_{\text{tot}} \simeq 24$ when $t_{\text{snr}} = 100 \text{ yr}$),⁸ and the gamma-ray band is dominated by pion-decay. The shock speed is high during this time and the downstream temperature, while very much less than the R-H value ($T_2 \simeq 3 \times 10^7 \text{ K}$ for the nonlinear shock at $t_{\text{snr}} = 100 \text{ yr}$ versus $T_2 \simeq 1.4 \times 10^9 \text{ K}$ for the test-particle shock!), is also high. The transition into the Sedov phase at $t_{\text{snr}} \sim 300 \text{ yr}$ brings about a steady decline in $T_{\text{p}2}$ along with a gamma-ray flux which is almost independent of SNR age, a property present in the more complex models of Dorfi

⁸Note that high Mach number *unmodified* shocks (i.e., those with $r_{\text{tot}} \simeq 4$) are possible as described in general by Berezhko & Ellison (1999) and specifically for SN1006 by Berezhko, Ksenofontov, & Petukhov (1999a) if injection rates lower than that assumed here are used.

(1991), Drury, Aharonian, & Völk (1994), Baring et al.(1999), and Berezhko & Völk (1997). The origin of this gamma-ray insensitivity to t_{snr} prior to a remnant’s radiative phase is an approximate compensation (Baring 2000) between the volume that scales as $t_{\text{snr}}^{6/5}$ (radius $\propto t_{\text{snr}}^{2/5}$) in the Sedov phase, and the shock speed (and therefore also the square root of T_{p2}) that declines as $t_{\text{snr}}^{-3/5}$ so that a roughly E^{-2} particle distribution function has a normalization that scales as $T_{\text{p2}} \propto t_{\text{snr}}^{-6/5}$. The contrast between the free expansion and Sedov phases is underlined by the change in shock parameters: at $t_{\text{snr}} = 30$ yr (solid curve) $V_{\text{sk}} = 1.4 \times 10^4$ km s $^{-1}$, $M_{\text{S0}} = 850$, $M_{\text{A0}} = 2.4 \times 10^3$, and $r_{\text{tot}} = 25$, while at $t_{\text{snr}} = 10^4$ yr (dotted curve), $V_{\text{sk}} = 490$ km s $^{-1}$, $M_{\text{S0}} = 31$, $M_{\text{A0}} = 90$, and $r_{\text{tot}} = 8.5$.

In Figure 7 we show, as a function of B_0 and n_{p0} , the following ratio:

$$R_{\text{phot}} = \frac{\frac{1}{E_0} \int_{E_0}^{\infty} F_{\nu} dE}{F_{\nu}(E = 10^{-11} \text{MeV})}, \quad (20)$$

that is, the integral photon flux above E_0 normalized to E_0 over the radio flux (F_{ν} has units of cm $^{-2}$ -s $^{-1}$ and we set $E_0 = 500$ GeV in Fig. 7). This ratio is critical for gamma-ray searches of radio SNRs and the most important result is that, for $n_{p0} \leq 1$ cm $^{-3}$, SNRs in high B_0 environments have the lowest R_{phot} . For n_{p0} held fixed at 0.01 cm $^{-3}$, R_{phot} decreases by more than two orders of magnitude as B_0 increases from 1 to 100 μ G. However, the absolute TeV flux depends strongly on the density as shown in Figure 5a.

Another critical factor for TeV observations involves the relative importance of inverse-Compton versus pion-decay emission and the impact this has on our ideas for the origin of cosmic rays. In Figure 8 we show the inverse-Compton and pion-decay components for the parameters marked with dots in Figure 7. The variation in total absolute flux for the three cases is relatively small but there is a shift from inverse-Compton being dominant at TeV energies when $n_{p0} = 0.01$ cm $^{-3}$ to pion-decay being dominant when $n_{p0} = 10$ cm $^{-3}$. In the high B_0 case, pion-decay emission extends to higher energies than the inverse-Compton because the electron spectrum is cutoff from synchrotron and inverse-Compton losses. Hence, atmospheric Čerenkov experiments may provide detections of pion decay emission in sources with high magnetic fields. This may be the case in the recent marginal detection (Völk et al. 2000) of Cas A by HEGRA. Yet the spectral shape in the TeV band bears no signature peculiar to pion-decay emission, but rather is a marker of the underlying particle distributions. Hence, the most powerful diagnostic the sensitive TeV experiments will provide is the determination of the maximum energy of emission, thereby constraining the ISM density, magnetic field and the electron to proton ratio.

3.2. SNR SN1006

For a concrete example, we apply our model to SN1006, the first remnant to have a detection of shell-related TeV gamma-ray emission reported, by the CANGAROO collaboration (Tanimori et al. 1998). We constrain our parameters to match those used by Berezhko, Ksenofontov, &

Petukhov (1999a) as closely as possible and discuss the comparison with that model below. A full listing of the parameters is given in Table 1 under the column labeled SN1006_{NL}, where the ‘NL’ subscript contrasts this nonlinear result with the test-particle one discussed in Section 3.3 below. The parameters used by Berezhko, Ksenofontov, & Petukhov are listed in the column labeled BKP99. In particular, we use an unshocked proton density $n_{p0} = 0.1 \text{ cm}^{-3}$, SN energy $E_{\text{sn}} = 10^{51} \text{ erg}$, ejecta mass $M_{\text{ej}} = 1.4M_{\odot}$ (i.e., values similar to those given by Truelove & McKee 1999 and/or Laming et al. 1996), and an ejecta density profile characterized by $n = 7$ (i.e., Eq. 16). For a remnant age $t_{\text{snr}} = 990 \text{ yr}$, these values yield $V_{\text{sk}} \simeq 3750 \text{ km s}^{-1}$ and $R_{\text{sk}} \simeq 7 \text{ pc}$ in the Truelove and McKee model. If we take the observed proper motion of $0''.30 \pm 0''.04 \text{ yr}^{-1}$ (Long et al. 1988), this speed yields a distance of 2.3 kpc, and using the observed angular size of $30'$, this implies an angular radius of 10 pc, within 50% of the 7 pc given above.

Figure 9 shows the continuum component photon spectra obtained from these parameters, along with the sum of the components (heavy solid line). In obtaining the normalization for this fit, the emission volume was taken to be $\sim 195 \text{ pc}^3$, i.e., the value given by Eq. (19) and the distance to the source was assumed to be $D_{\text{snr}} = 1.7 \text{ kpc}$, commensurate with that deduced from optical observations (see Green 1998, and references therein). If we had taken $D_{\text{snr}} = 2.3 \text{ kpc}$, the required emission volume would be correspondingly larger to match the observed flux. It’s clear that a reasonable fit to the observed spectra is produced considering that we used the same parameters as Berezhko, Ksenofontov, & Petukhov.⁹ Note that we have not included free-free absorption in our models.

Our results indicate that the TeV emission in SN1006 is dominated by the inverse-Compton component, in general agreement with the conclusions of previous work that invoke test-particle power-laws, i.e., Mastichiadis & de Jager (1996) and Tanimori et al. (1998). However, there is a pion-decay component at TeV energies and small changes in the parameters can make it more pronounced than shown in Fig. 9, as indicated in the results of Berezhko, Ksenofontov, & Petukhov (1999a,b) discussed below. Also in agreement with previous work (e.g., Koyama et al. 1995; Reynolds 1996), the X-ray emission is dominated by synchrotron emission from super-TeV electrons. However, bremsstrahlung does contribute some at hard X-ray energies and again, this contribution is sensitive to the input parameters. The result shown in Figure 9 assumes $T_{e2}/T_{p2} = 1$. AXAF and XMM will probe the X-ray emission at and below the ASCA data range depicted in Figure 9, and the INTEGRAL experiment will be sensitive to the hard X-ray band below 200 keV. Together, these spacecraft should be able to clearly differentiate the synchrotron and bremsstrahlung components in the X-ray range and, therefore, provide constraints for the entire broad-band emission.

⁹We have used $\alpha = 0.6$ for this fit. Berezhko, Ksenofontov, & Petukhov (1999a) and Ammosov et al. (1994) found that a similar value ($\alpha = 0.5$) was required for a good fit and Reynolds (1996) gave a detailed explanation of why such a broadening might occur for the electron spectrum.

3.2.1. Comparison with the Kinetic NL Model of Berezhko et al.

As mentioned above, Berezhko, Ksenofontov, & Petukhov (1999a,1999b) have presented results for SN1006 using a kinetic, nonlinear model of diffusive cosmic ray acceleration by a spherically symmetric, expanding SNR. This model self-consistently solves the cosmic ray transport equations together with the gas dynamic equations and is based on the work of Berezhko et al. (1996) and Berezhko & Völk (1997). It is more complete than the steady-state, plane-shock model presented here and keeps track of the accelerated particles as the SNR evolves and yields the integrated emission over the entire remnant as a function of time including adiabatic losses. It also considers the diffusive properties of the particles as a function of energy so that low energy electrons responsible for the radio emission occupy a thin region behind the forward shock, while the highest energy particles fill the entire volume behind the shock. Despite these substantial differences, both models produce good fits to the broad-band continuum with virtually identical input parameters. The Berezhko, Ksenofontov, & Petukhov parameters are listed in Table 1 under the heading ‘BKP99.’

The only difference in the input parameters is the small difference in α , all other input parameters are the same. Note that the proton injection rate we use ($\eta_{\text{inj,p}} = 2.1 \times 10^{-4}$) is equivalent to the value ($\eta_{\text{inj,p}} = 5 \times 10^{-4}$) used by Berezhko, Ksenofontov, & Petukhov, since injection is treated somewhat differently in the two models and these two values give the same injection efficiency. The output parameters, as indicated in Table 1, differ only slightly and in Figure 10 we compare the shapes of the proton distributions for the two models. The most obvious difference is the lack of a thermal peak in the Berezhko et al. result (solid curve). They inject particles at a superthermal momentum (i.e., at p_{inj} as given in Eqn. 1) and do not model thermal particles. However, they could have included a shock heated thermal distribution as we do here, in which case it would have been very similar to the dashed curve since both models have similar pre-shock and injection conditions. The good correspondence in shape over the entire superthermal range occurs despite the fact that the plane-shock, simple model is steady-state and uses the shock conditions at the SNR age (as determined by the Truelove & McKee parameterization) to determine the emission at that instant. In contrast, the Berezhko et al. model is fully time-dependent and integrates the emission over the remnant. Notably, the spectral curvature typical of nonlinear shock acceleration survives the volume integration in the Berezhko et al. result.

The two models do differ somewhat in the fraction of TeV flux contributed by pion-decay. Berezhko, Ksenofontov, & Petukhov find that pion-decay and inverse-Compton contribute about equally while here, inverse-Compton is clearly dominant. While these differences and other effects will be considered with more detailed comparisons in future work, we believe this example gives credence to our claim that the simple model is getting the basic physics correct. Furthermore, the added ability to provide rapid, broad-band fitting is very important because it is simply not possible, because of computing limitations, to perform a comprehensive parameter search with complicated codes such as the Monte Carlo technique used in Baring et al. (1999) in a timely manner. Our model does permit such a search, and we anticipate it can be used to significant advantage in astronomical data analysis packages, providing the capability, not previously available,

for incorporating the principal nonlinear effects of shock acceleration.

3.3. Test-particle vs. nonlinear results

As we mentioned above, despite considerable evidence to the contrary, many astrophysical applications of diffusive shock acceleration still assume that the acceleration is inefficient and produces test-particle power laws.¹⁰ A high efficiency for producing cosmic rays will have far-reaching consequences for a number of applications because values for the shocked temperature and density will differ from the test-particle Rankine-Hugoniot values. This will be particularly important for X-ray line emission models. To illustrate how the predictions of diffusive shock acceleration vary depending on whether the test-particle or nonlinear assumption is made, we show in Figure 11 (light-weight curves) the phase-space electron and proton distributions that produced the emission shown in Figure 9. These are compared to test-particle spectra (heavy-weight curves) calculated for parameters which are the same except the proton injection efficiency is set to $\eta_{\text{inj,p}} = 1 \times 10^{-5}$ in the test-particle case.

For the test-particle case (column labeled SN1006_{TP} in Table 1): $r_{\text{tot}} = 4.1$, $r_{\text{sub}} = 4.0$, and $T_2 \simeq 1.7 \times 10^8$ K, while for the nonlinear case: $r_{\text{tot}} = 7.2$, $r_{\text{sub}} = 3.6$, and $T_2 \simeq 4.7 \times 10^7$ K. In the nonlinear case, the shocked density is $\sim 75\%$ *greater* and the shocked temperature is more than a factor of 3 *less* than the test-particle result. Furthermore, the nonlinear electron spectrum in Figure 11 shows a stronger nonthermal tail on the thermal peak (comparison between the dotted and dot-dashed curves in Figure 2 gives a much more extreme example). Accurate electron temperatures and knowledge of the presence of significant nonthermal electron distributions are of prime importance for modeling X-ray line emission from shock heated gas (e.g., Hamilton et al. 1983). Line models depend strongly on the assumed electron temperature and density and may change substantially if cosmic rays are accelerated with efficiencies typical of the example just given. Dorfi & Böhringer (1993) (see also Dorfi 1994) calculate the evolution of SNRs including cosmic ray production and find examples where $\gtrsim 50\%$ of the explosion energy is transferred to cosmic rays, reducing the X-ray emission by a factor of 20 from test-particle predictions. Efficiencies nearly this high are found by Berezhko, Ksenofontov, & Petukhov (1999a,1999b) and are typical of those shown here in Table 1.

The four-component sum of the photon emission from the test-particle result for SN1006 is shown as the heavy dotted curve in Figure 9 where the emission volume has been adjusted to fit the radio flux. The broad-band fit is unsatisfactory and does not improve substantially if parameters other than $\eta_{\text{inj,p}}$ are varied. In the test-particle result, the X-ray emission is dominated by thermal bremsstrahlung and the TeV to radio flux ratio is much smaller than in the nonlinear result.

¹⁰Of course, many examples exist of full nonlinear calculations of SNR evolution (e.g., Dorfi & Völk 1996; Berezhko et al. 1999b; Kang & Jones 1995), but despite this, we believe the importance of nonlinear effects has been slow to reach the general astrophysical community.

4. SUMMARY AND CONCLUSIONS

We have developed a computationally fast and easy-to-use model of nonlinear diffusive shock acceleration along with the accompanying photon emission from the resultant electron and ion spectra. Using this model, we showed how the emission depends on both model and environmental parameters and identified ambient density and magnetic field as being the most important in determining the broad-band emission. We also showed that our simple model is in excellent agreement with a more complete and complex model of the supernova remnant SN1006.

A particularly important aspect of nonlinear acceleration is that shock *heating* is linked to particle acceleration and thus to the broad-band photon emission. As shown in Figures 2, 4a, and 11, shocks which accelerate particles efficiently have lower postshock temperatures and higher postshock densities than test-particle predictions. Nonlinear shocks also produce electron spectra with superthermal tails (Figures 2, 3, and 11). These factors are important for X-ray line emission (e.g., Dorfi & Böhringer 1993) and open up the possibility of using radio, X-ray continuum, and γ -ray observations to constrain X-ray line models and vice versa. We believe the model we present here is a first step in this process.

To describe SNRs, we use a model of an expanding, spherical shock wave (Truelove & McKee 1999) to obtain shock parameters as a function of SNR parameters and time. Using these parameters, we calculate nonlinear particle spectra and produce “snapshot” continuum photon spectra from synchrotron, bremsstrahlung, inverse-Compton, and pion-decay, spanning the range from radio to TeV γ -rays. More realistic models would include inhomogeneous ejecta, emission from dense clumps, pre-SN winds, a reverse shock, volume integrated emission from regions undergoing adiabatic cooling, oblique shock geometry, and effects on the SNR evolution from particle escape (or dilution). Some of these additions have already been performed by Berezhko, Ksenofontov, & Petukhov (1999a) and our results are in excellent agreement with theirs for SN1006 (Figure 9 and Section 3.2.1), some can be added easily to the simple model, but others (such as oblique geometry) are much more difficult. Despite this, we believe this nonlinear model is accurate enough to approximate expected emission fluxes and clearly track important trends as we describe in detail in Section 3.1.2.

Nonlinear shock acceleration unavoidably involves a large number of model and environmental parameters and it is essential to know how they relate to each other and which ones have the greatest impact on the results. Of the model parameters, the injection efficiency, $\eta_{\text{inj,p}}$, has the greatest influence on the solutions since it sets the overall efficiency and determines whether the acceleration is nonlinear or can be treated as test particle (Figures 2 and 4a). Unfortunately, $\eta_{\text{inj,p}}$ is not well constrained by theory and heliospheric observations remain limited; in fact, there’s virtually no constraining information on the efficiency of high Mach number shocks like those expected in young SNRs. However, the differences between test-particle and nonlinear predictions are so large in both the broad-band continuum and the X-ray line emission, that we believe it will be possible to set strong constraints on the acceleration efficiency once nonlinear models of

X-ray line emission become available. Other model parameters, such as the ratios of shocked electron to proton temperature and of electron to proton acceleration efficiency, are less fundamental but produce characteristic differences in the emission which can be constrained with sufficiently complete models and observations (Figures 4b and c).

The environmental parameters include the ambient interstellar proton density n_{p0} and density profile, the magnetic field B_0 , the ejecta mass and density profile, supernova explosion energy, etc. Of these, the ambient density and magnetic field have, by far, the largest effect on the broad-band emission. As we show in Figures 3, 5, and 7, varying n_{p0} and B_0 produce a complicated set of changes in the emission which cannot be simply characterized. If density is held constant, the intensity in the radio band scales roughly as $B_0^{3/2}$, but at photon energies $E > \text{MeV}$, the intensity can decrease with increasing B_0 due to nonlinear effects (Figure 5b) and a weakening of the shock (i.e., decrease in the Alfvén Mach number). Likewise, when B_0 is fixed, an increase in density generally causes an increase in emission in the MeV range, but the emission in the radio band is relatively insensitive to density (Figure 5a). At TeV energies, the maximum photon energy increases as n_{p0} is decreased and, in general, the highest photon energies are obtained with the largest B_0 and the lowest n_{p0} . The TeV/radio flux ratio, however, is greatest for low ambient magnetic fields (Figure 7) and this is an important parameter if radio SNRs are selected for hard γ -ray searches. As we show in Figure 8, the distinctive pion-decay bump will be most prominent for remnants in high n_{p0} and high B_0 environments; given the flux levels predicted, we anticipate positive detections of such spectral features (generally below EGRET sensitivities for $n \lesssim 10 \text{ cm}^{-3}$), by the GLAST experiment in the not too distant future. While TeV experiments cannot probe such spectral features, they can detect the upper range of pion decay emission in remnants in high B_0 surroundings; this situation may already be realized in the recent announcement (Völk et al. 2000) of a positive detection of Cas A by HEGRA.

The nature of the X-ray emission also depends importantly on density and magnetic field. As density is increased at a given B_0 , the keV X-ray emission goes from being totally dominated by synchrotron from relativistic electrons to quasi-thermal bremsstrahlung emission. Note that the bremsstrahlung dominates even in the radio band for $n_{p0} = 10 \text{ cm}^{-3}$ and $B_0 = 3 \mu\text{G}$ (Fig. 5a). Similarly, at a given density (Figure 5b), the X-ray emission goes from being thermal bremsstrahlung to synchrotron as B_0 increases. If synchrotron is dominant, X-ray lines will be weak or absent so these differences are readily distinguishable observationally.

Finally, we suggest that the most important aspect of modeling photon emission from astrophysical shocks depends on whether or not the acceleration is efficient and nonlinear or inefficient and test-particle in nature. These situations can be quite different and if the acceleration is nonlinear, all parameters are interconnected and observations in any energy band limit the freedom to vary parameters in all other bands. Since there are a large number of parameters, understanding the nonlinear interactions requires a model that can efficiently map parameter space. We believe the model presented here, while not a replacement for more complete models, can do this expediently and accurately and be an aid in interpreting the vast amount of information expected from

current and future space and ground-based telescopes.

Acknowledgments: We wish to thank John Raymond for providing information concerning SN1006. We also thank Rod Lessard for providing Veritas flux sensitivity data and Anne Decourchelle for helpful discussions. This work was performed, in part, with support from NASA's Space Physics Theory Program.

REFERENCES

- Achterberg, A., Blandford, R.D., Reynolds, S.P. 1994, *A.A.*, 281, 220
- Ammosov, A.E., Ksenofontov, L.T., Nikolaev, V.S., & Petukhov, S.I. 1994, *Astronomy Letters.*, 22, 151
- Axford, W.I., Leer, E., & Skadron, G. 1977, in *Proc. 15th ICRC (Plovdiv)*, 11, 132
- Baring, M. G. 2000, in *Proceedings of the Snowbird TeV Gamma-Ray Workshop*, eds. B. L. Dingus et al. (AIP, New York)
- Baring, M.G., Ogilvie, K.W., Ellison, D.C., & Forsyth, R.J. 1997, *Ap.J.*, 476, 889
- Baring, M.G., Ellison, D.C., Reynolds, S.P., Grenier, I.A., & Goret, P. 1999, *Ap.J.*, 513, 311
- Baring, M. G., Jones, F. C., & Ellison, D. C. 2000, *Ap. J.* in press.
- Bell, A.R. 1978, *M.N.R.A.S.*, 182, 147
- Berezhko, E.G. 1996, *Astroparticle Phys.*, 5, 367
- Berezhko, E.G., Ellison, D.C. 1999, *Ap.J.*, 526, 385
- Berezhko, E.G., Krymsky, G.F. 1988, *Sov. Phys. Usp.*, 31, 27
- Berezhko, E. G., & Ksenofontov, L.T. 1999, *Proc. 26th Int. Cosmic Ray Conf. (Salt Lake City)*, 4, 381
- Berezhko, E. G., Ksenofontov, L.T., & Petukhov, S. I. 1999a, *Proc. 26th Int. Cosmic Ray Conf. (Salt Lake City)*, 4, 431
- Berezhko, E. G., Ksenofontov, L., & Petukhov, S. I. 1999b, in press.
- Berezhko, E.G., Yelshin, V.K., & Ksenofontov, L.T. 1996, *JETP*, 82(1), 1
- Berezhko, E.G., & Völk, H.J. 1997, *Astroparticle Phys.*, 7, 183

- Blandford, R.D., & Eichler, D. 1987, *Phys. Repts.*, 154, 1
- Blandford, R.D., & Ostriker, J.P. 1978, *Ap.J.(Letts)*, 221, L29
- Bykov, A.M., Chevalier, R.A., Ellison, D.C., & Uvarov, Yu.A. 2000, *Ap. J.*, in press
- Chevalier, R.A. 1982, *Ap.J.*, 258, 790
- de Jager, O. C., Harding, A. K., Michelson, P. F., Nel, H. I., Nolan, P. L., Sreekumar, P., & Thompson, D. J. 1996, *Ap.J.*, 457, 253
- de Jager, O. C., & Mastichiadis, A. 1997, *Ap.J.*, 482, 874
- Dorfi, E. A. 1991, *A.A.*, 251, 597.
- Dorfi, E. A. 1994, *Ap.J.Suppl.*, 90, 841
- Dorfi, E.A., & Böhringer, H. 1993, *A.A.*, 273, 251
- Dorfi, E.A., & Völk, H.J. 1996, *A.A.*, 307, 715
- Drury, L.O’C. 1983, *Rep. Prog. Phys.*, 46, 973
- Drury, L.O’C., Aharonian, F.A., & Völk, H.J. 1994, *A.A.*, 287, 959
- Eichler, D. 1981, *Ap.J.*, 247, 1089
- Eichler, D. 1984, *Ap.J.*, 277, 429
- Ellison, D.C. 2000, *Proc. of ACE workshop*, in press
- Ellison, D.C., Baring, M.G., & Jones, F.C. 1996, *Ap.J.*, 473, 1029
- Ellison, D.C., & Berezhko, E.G. 1999a, *Proc. 26th Int. Cosmic Ray Conf. (Salt Lake City)*, 4, 390
- Ellison, D.C., & Berezhko, E.G. 1999b, *Proc. 26th Int. Cosmic Ray Conf. (Salt Lake City)*, 4, 446
- Ellison, D.C., & Eichler, D. 1984, *Ap.J.*, 286, 691
- Ellison, D.C., Möbius, E., & Paschmann, G. 1990, *Ap.J.*, 352, 376
- Gaisser, T. K., Protheroe, R. J., & Stanev, T. 1998, *Ap.J.*, 492, 219
- Gehrels, N. & Michelson, P. 1999, *Astroparticle Phys.*, 11, 277.
- Giacalone, J., Burgess, D., Schwartz, S.J., & Ellison, D.C. 1993, *Ap.J.*, 402, 550
- Giacalone, J., Burgess, D., Schwartz, S.J., Ellison, D.C., & Bennett, L. 1997, *J.G.R.*, 102, 19,789
- Gosling, J.T., Asbridge, J.R., Bame, S.J., Feldman, W.C., Zwickl, R.D., Paschmann, G., Sckopke, N., & Hynds, R.J. 1981, *J.G.R.*, 86, 547

- Green, D. A., A Catalogue of Galactic Supernova Remnants (1998 September version),
[<http://www.mrao.cam.ac.uk/surveys/snrs/>]
- Hamilton, A.J.S., Sarazin, C.L., & Chevalier, R.A. 1983, *Ap.J.Suppl.*, 51, 115
- Jones, F. C., & Ellison, D. C. 1991, *Space Sci. Rev.*, 58, 259
- Kang, H. & Jones, T. W. 1991, *M.N.R.A.S.*, 249, 439
- Kang, H. & Jones, T. W. 1995, *Ap.J.*, 447, 944
- Kennel, C.F., Edmiston, J.P., Scarf, F.L., Coroniti, F.V., Russell, C.T., Smith, E.J., Tsurutani, B.T., Scudder, J.D., Feldman, W.C., Anderson, R.R., Moser, F.S., & Temerin, M. 1984, *J.G.R.*, 89, 5436
- Kohnle, A. et al. 1999, *Proc. 26th Int. Cosmic Ray Conf. (Salt Lake City)*, 5, 239
- Koyama, K. et al. 1999, *Nature*, 378, 255
- Krymskii, G.F. 1977, *Sov. Phys. Dokl.*, 22(6), 327
- Laming, J., M., Raymond, J.C., McLaughlin, B.M., & Blair, W.P. 1996, *Ap.J.*, 472, 267
- Lee, M.A. 1982, *J.G.R.*, 87, 5063
- Lee, M.A. 1983, *J.G.R.*, 88, 6109
- Levinson, A. 1992, *Ap.J.*, 401, 73
- Levinson, A. 1994, *Ap.J.*, 426, 327
- Long,, K.S., Blair, W.P., & van den Bergh, S. 1988, *Ap.J.*, 333, 749
- Lorenz, E. 1997, in *Towards a Major Atmospheric Čerenkov Detector*, ed. O. C. de Jager (Wesprint, Pochefstroom) p. 415.
- Malkov, M.A. 1997, *Ap.J.*, 485, 638
- Malkov, M.A. 1999, *Ap.J.(Letts)*, 511, L53
- Mastichiadis, A. & de Jager, O. C. 1996, *A.A.*, 311, L5
- Müller, D., & Tang, K.-K. 1987, *Ap.J.*, 312, 183
- Müller, D., et al. 1995, in *Proc. 24th ICRC(Rome)*, 3, 13
- Reynolds, S.P. 1996, *Ap.J.(Letts)*, 459, L13
- Reynolds, S.P., & Ellison, D.C. 1992, *Ap.J.(Letts)*, 399, L75

- Rybicki, G.B., & Lightman, A.P. 1979, “Radiative Processes in Astrophysics,” John Wiley & Sons, New York.
- Scholer, M., Kucharek, H., & Giacalone, J. 2000, J.G.R., in press
- Scholer, M., Trattner, K.J., & Kucharek, H. 1992, Ap.J., 395, 675
- Sturmer, S. J., Skibo, J. G., Dermer, C. D., & Mattox, J. R. 1997, Ap.J., 490, 619
- Tanimori, T., et al. 1998, Ap.J.(Letts), 497, L25
- Terasawa, T., et al. 1999, Proc. 26th Int. Cosmic Ray Conf. (Salt Lake City), 6, 528
- Truelove, J.K., & McKee, C.F. 1999, Ap.J.Suppl., 120, 299
- Völk, H. J., et al. 2000, in Proceedings of the Snowbird TeV Gamma-Ray Workshop, eds. B. L. Dingus et al. (AIP, New York)
- Weekes, T. C., et al. 1999, VERITAS proposal [<http://egret.sao.arizona.edu/vhegra/vhegra.html>]
- Zimmermann, H. U., Trümper, J. E., & Yorke, H. 1996, Röntgenstrahlung from the Universe, MPE Report 263 (Max-Planck-Institut für Extraterrestrische Physik, Garching)

TABLE 1
Parameters for Figure 3 and SN1006

Input parameters	Low	High	SN1006 _{NL}	BKP99 ⁵	SN1006 _{TP}
n_{p0} [cm ⁻³] ¹	0.01	10	0.1	0.1	0.1
B_0 [μG]	3	30	9	9	9
B_2 [μG] ²	3	30	30	30	30
t_{snr} [yr]	1000	1000	990	990	990
E_{sn} [10 ⁵¹ erg]	1	1	1	1	1
M_{ej} [M_{\odot}]	1	5	1.4	1.4	1.4
T_{p0} [K]	10 ⁴	10 ⁴	10 ⁴	10 ⁴	10 ⁴
T_{e2}/T_{p2}	1	1	1	—	1
$\eta_{\text{inj,p}}$ ³	10 ⁻³	10 ⁻³	2.1×10^{-4}	5×10^{-4}	1×10^{-5}
$(e/p)_{\text{rel}}$	0.03	0.03	2×10^{-3}	2×10^{-3}	2×10^{-3}
η_{mfp}	1	1	13	—	13
α	1	1	0.6	0.5	0.6
n	0	0	7	7	7
Output values					
M_{S0}	400	85	235	170	235
M_{A0}	120	77	72	67	72
V_{sk} [km s ⁻¹]	6400	1350	3750	3520	3750
R_{sk} [pc]	11	3.0	7.0	6.9	7.0
r_{tot}	9.7	8.5	7.2	6.7	4.1
r_{sub}	3.0	2.9	3.6	3.6	4.0
$E_{\text{max,p}}$ [TeV]	30	16	9	10	11
$E_{\text{max,e}}$ [TeV]	30	12	9	10	10
$\eta_{\text{inj,e}}$	5×10^{-3}	0.11	2.9×10^{-5}	—	8×10^{-7}
T_{p2} [K]	6.4×10^7	3.6×10^6	4.7×10^7	—	1.7×10^8
T_{tp} [K] ⁴	5.0×10^8	2.2×10^7	1.7×10^8	—	1.7×10^8
ϵ_{rel}	0.80	0.75	0.63	0.40	0.02
Flux parameters					
D_{snr} [kpc]	1	1	1.7	1.7	1.7
V_{emis} [pc ³]	1	1	195 ⁶	—	5×10^3 ⁷

¹ This is the unshocked proton density. In all cases, including our match to the Berezhko, Ksenofontov, & Petukhov example, a helium number density of $0.1 n_{p0}$ is assumed.

² In order to compare our model to that of Berezhko, Ksenofontov, & Petukhov (1999a), we include a compressed downstream magnetic field for purposes of calculating the synchrotron

emission from SN1006. In all other results we take $B_2 = B_0$.

³ See the discussion in Section 3.2.1 concerning this parameter and the Berezhko, Ksenofontov, & Petukhov results.

⁴ This is the temperature of the shocked gas in the test-particle approximation.

⁵ The parameters given here are for the model shown as a solid line in Figure 1d of Berezhko, Ksenofontov, & Petukhov (1999a).

⁶ This value is that given in Eqn. (19).

⁷ This value is ~ 15 times V_{emis} given in Eqn. (19).

TABLE 2
Parameters for Figure 5

Input	(a)				(b)			
	solid	dashed	dot-dashed	dotted	solid	dashed	dot-dashed	dotted
n_{p0} [cm^{-3}]	0.01	0.1	1	10	1	1	1	1
B_0 [μG]	3	3	3	3	3	10	30	100
t_{snr} [yr]	1000	1000	1000	1000	1000	1000	1000	1000
E_{sn} [10^{51} erg]	1	1	1	1	1	1	1	1
M_{ej} [M_{\odot}]	1	1	1	1	1	1	1	1
T_{p0} [K]	10^4	10^4	10^4	10^4	10^4	10^4	10^4	10^4
T_{e2}/T_{p2}	1	1	1	1	1	1	1	1
$\eta_{\text{inj,p}}$	10^{-3}	10^{-3}	10^{-3}	10^{-3}	10^{-3}	10^{-3}	10^{-3}	10^{-3}
$(e/p)_{\text{rel}}$	0.03	0.03	0.03	0.03	0.03	0.03	0.03	0.03
Output								
M_{S0}	400	220	130	79	130	130	130	130
M_{A0}	110	200	370	720	370	110	37	11
V_{sk} [km s^{-1}]	6340	3440	2050	1260	2050	2050	2050	2050
R_{sk} [pc]	10.5	7.4	4.8	3.1	4.8	4.8	4.8	4.8
r_{tot}	9.6	12	14	17	14	9.6	6.7	4.8
r_{sub}	3.0	3.0	3.0	3.0	3.0	2.9	3.0	3.2
$E_{\text{max,p}}$ [TeV]	32	8	2.4	0.8	2.4	11	44	180
$E_{\text{max,e}}$ [TeV]	32	8	2.4	0.8	2.4	11	20	12
$\eta_{\text{inj,e}}$	5×10^{-3}	0.035	6×10^{-3}	7×10^{-3}	6×10^{-3}	9×10^{-3}	0.011	0.013
T_{p2} [K]	6.3×10^7	1.3×10^7	3.0×10^6	7.8×10^5	3.0×10^6	6.6×10^6	1.3×10^7	2.8×10^7
T_{tp} [K]	4.9×10^8	1.5×10^8	5.1×10^7	1.9×10^7	5.1×10^7	5.1×10^7	5.1×10^7	5.1×10^7
ϵ_{rel}	0.81	0.85	0.88	0.90	0.88	0.79	0.63	0.37
Flux								
D_{snr} [kpc]	1	1	1	1	1	1	1	1
V_{emis} [pc^3]	510	140	33	7.2	33	50	70	100

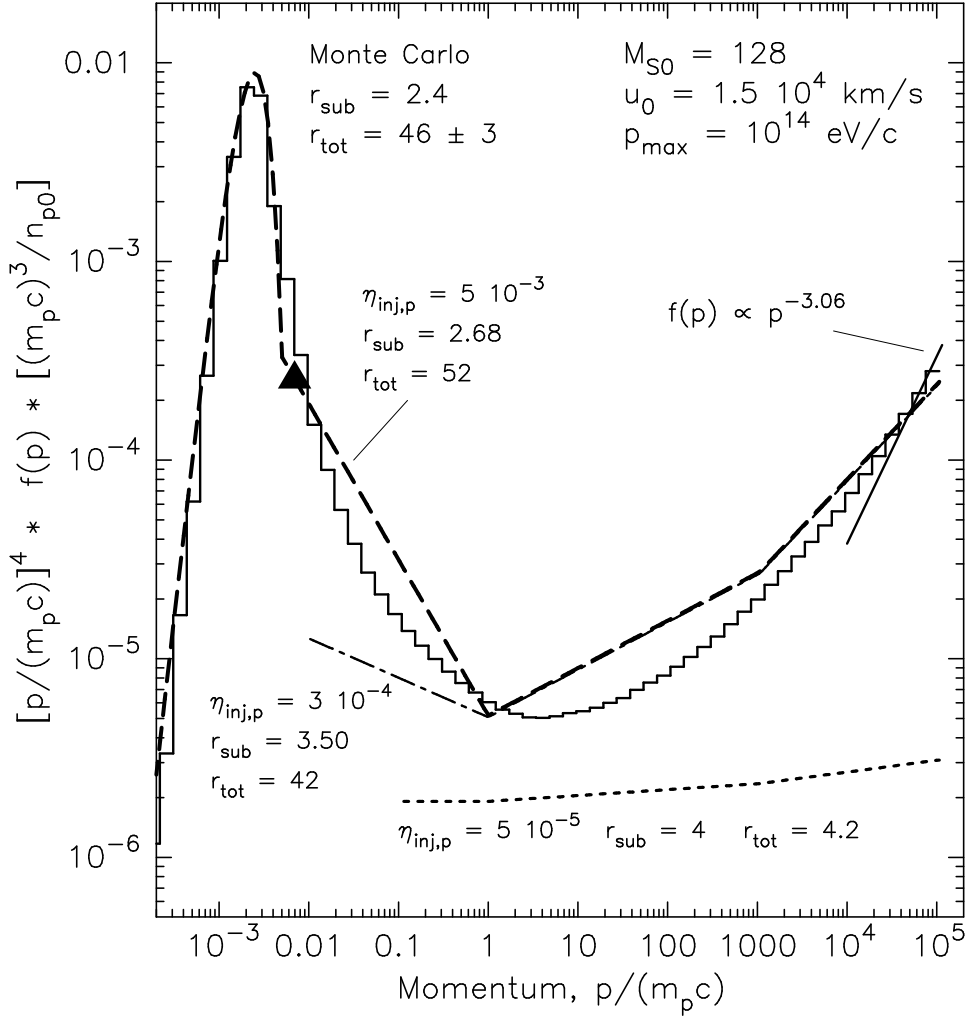


Fig. 1.— Downstream phase space distribution functions, f , versus momentum, p . We have multiplied $f(p)$ by $[p/(m_p c)]^4$ to flatten the spectra, and by $[(m_p c)^3/n_{p0}]$ to make them dimensionless. The solid histogram is a Monte Carlo model result, while the dashed, dot-dashed, and dotted curves are from the simple model. The three simple model results are obtained with identical input parameters except for $\eta_{inj,p}$ which is varied as shown. The $\eta_{inj,p} = 5 \times 10^{-3}$ case is chosen to match the Monte Carlo result and a good correspondence between the two models is obtained above the injection momentum, $p_{inj} \simeq 7 \times 10^{-3} m_p c$. The injection momentum, p_{inj} , varies with input parameters: for $\eta_{inj,p} = 3 \times 10^{-4}$, $p_{inj} \simeq 1.0 \times 10^{-2} m_p c$, and for $\eta_{inj,p} = 5 \times 10^{-5}$, $p_{inj} \simeq 0.11 m_p c$. As explained in Berezhko & Ellison (1999), the model spectra are considerably steeper than the test-particle prediction for $r_{tot} = 46$, $f \propto p^{-3.06}$ (solid line), at the highest momenta.

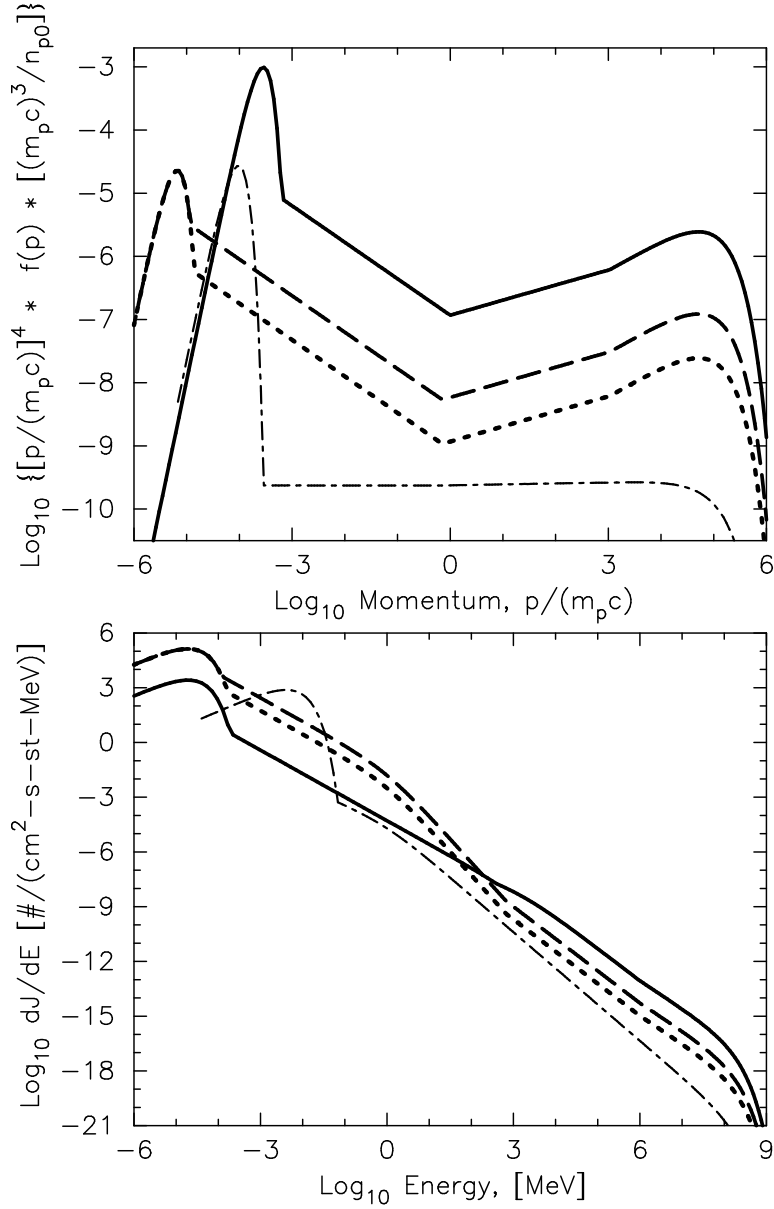


Fig. 2.— Top panel: Phase space distribution functions, $f(p)$, flattened and made dimensionless as in Fig. 1. The solid curve shows protons, the dashed curve shows electrons with $(e/p)_{\text{rel}} = 0.05$, and the dotted curve shows electrons with $(e/p)_{\text{rel}} = 0.01$. No synchrotron or inverse-Compton losses are included so the electron and proton spectra cutoff at the same momentum. Bottom panel: Differential energy flux distributions for the same particles. These spectral are normalized with a far upstream number density, n'_0 , such that $n'_0 u_0 = 1 \text{ cm}^{-2} \text{ s}^{-1}$. The dot-dashed curves are test-particle electron results with $(e/p)_{\text{rel}} = 0.01$ included for comparison. All input parameters are the same as for the dotted curves except $\eta_{\text{inj,p}} = 5 \times 10^{-6}$ which gives $r_{\text{tot}} = 4.1$.

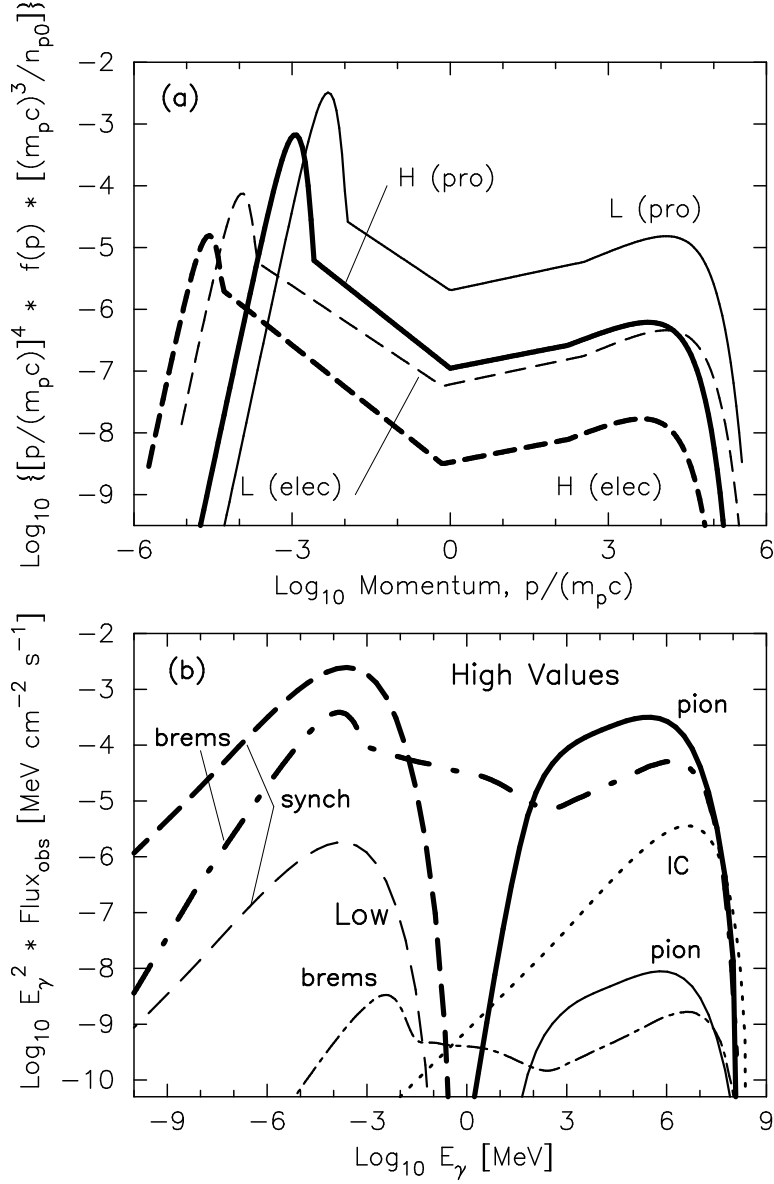


Fig. 3.— Top panel: Phase space distributions for a parameter set with low values of n_{p0} , M_{ej} , and B_0 (light-weight curves) and high values (heavy-weight curves). The protons are shown as solid curves and the electrons are shown as dashed curves. Bottom panel: Photon fluxes at Earth from the distributions in the top panel assuming an emission volume of $V_{\text{emis}} = 1 \text{ pc}^3$ at a distance of 1 kpc. In each case, the synchrotron emission is shown with a dashed curve, the bremsstrahlung with a dot-dashed curve, the inverse-Compton with a dotted curve, and the pion-decay with a solid curve. The inverse-Compton emission for the high value example is insignificant and is not shown. The full set of parameters for these models is given in Table 1 under columns marked ‘High’ and ‘Low.’

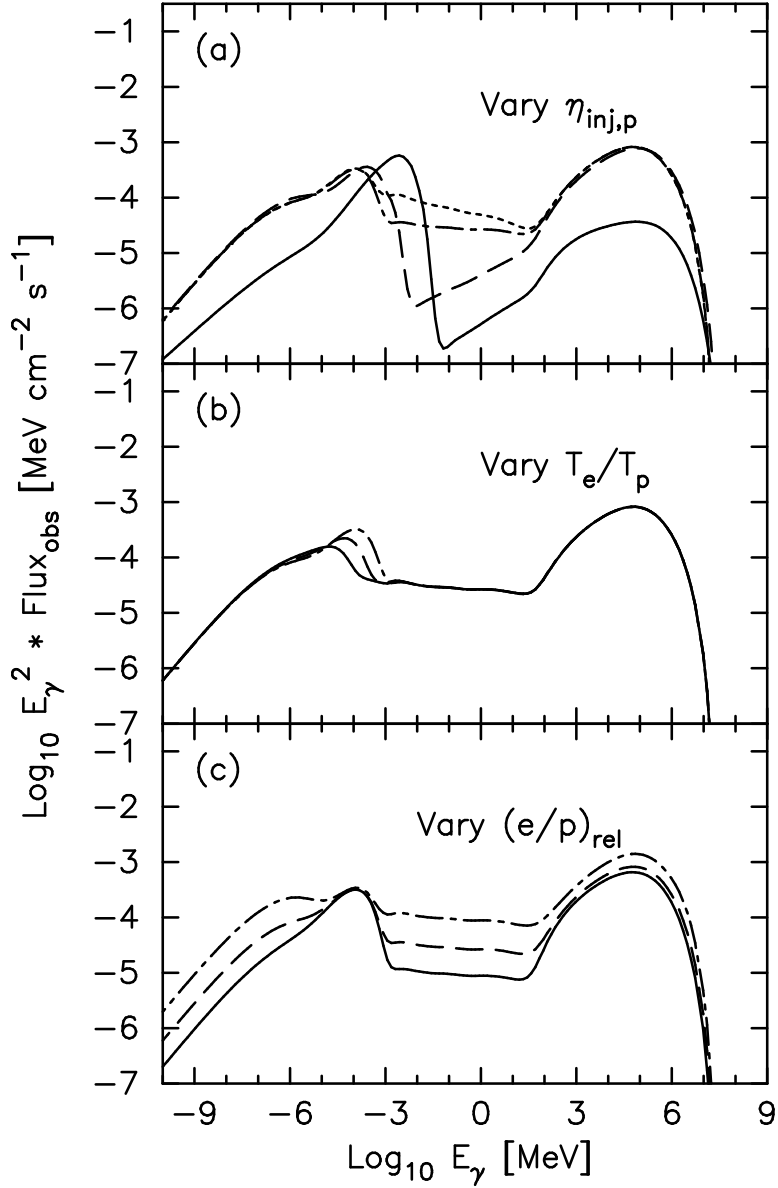


Fig. 4.— Total photon emission for various model parameters. In (a), $\eta_{\text{inj},p} = 1 \times 10^{-5}$ (solid), 1×10^{-4} (dashed), 1×10^{-3} (dot-dashed), and 2×10^{-3} (dotted) all with $T_{e2}/T_{p2} = 1$ and $(e/p)_{\text{rel}} = 0.03$. In (b): $T_{e2}/T_{p2} = 0.1$ (solid), 0.3 (dashed), and 1 (dot-dashed) all with $\eta_{\text{inj},p} = 1 \times 10^{-3}$ and $(e/p)_{\text{rel}} = 0.03$. In (c): $(e/p)_{\text{rel}} = 0.01$ (solid), 0.03 (dashed), and 0.1 (dot-dashed) all with $\eta_{\text{inj},p} = 1 \times 10^{-3}$ and $T_{e2}/T_{p2} = 1$. In all cases, $n_{p0} = 1 \text{ cm}^{-3}$, $B_0 = 3 \text{ } \mu\text{G}$, $E_{\text{sn}} = 1 \times 10^{51} \text{ erg}$, $M_{\text{ej}} = 1 M_{\odot}$, and $t_{\text{snr}} = 10^3 \text{ yr}$. Note that the vertical axis is proportional to the standard νF_{ν} representation.

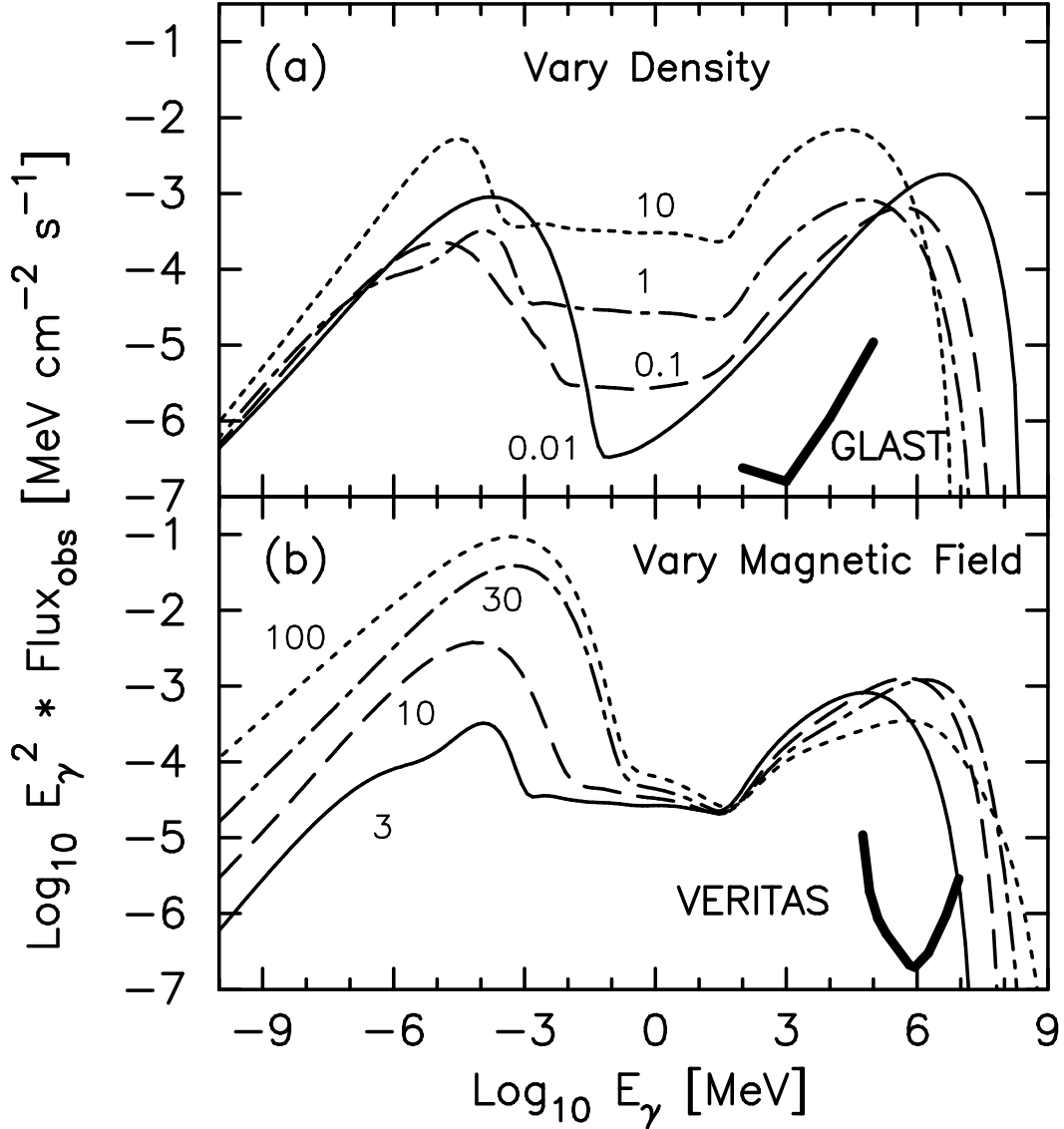


Fig. 5.— Total photon emission for various input parameters. In (a), the ISM field is fixed at $B_0 = 3 \mu\text{G}$ and the ambient number density is varied such that: $n_{p0} = 0.01 \text{ cm}^{-3}$ (solid), 0.1 cm^{-3} (dashed), 1 cm^{-3} (dot-dashed), and 10 cm^{-3} (dotted). In (b), B_0 is varied: $B_0 = 3 \mu\text{G}$ (solid), $10 \mu\text{G}$ (dashed), $30 \mu\text{G}$ (dot-dashed), and $100 \mu\text{G}$ (dotted), with the density pinned to $n_{p0} = 1 \text{ cm}^{-3}$. The input and output parameters for these examples are given in Table 2, but in all cases, $\eta_{\text{inj,p}} = 10^{-3}$, $T_{e2}/T_{p2} = 1$, $(e/p)_{\text{rel}} = 0.03$, $E_{\text{sn}} = 10^{51} \text{ erg}$, $M_{\text{ej}} = 1M_\odot$, $t_{\text{snr}} = 1000 \text{ yr}$, $\alpha = 1$, $\eta_{\text{mfp}} = 1$, and the flux at Earth is determined assuming $D_{\text{snr}} = 1 \text{ kpc}$ and an emission volume given by Eqn. (19). Also depicted are the canonical integral flux sensitivities for Veritas and GLAST (e.g., Weekes et al. 1999).

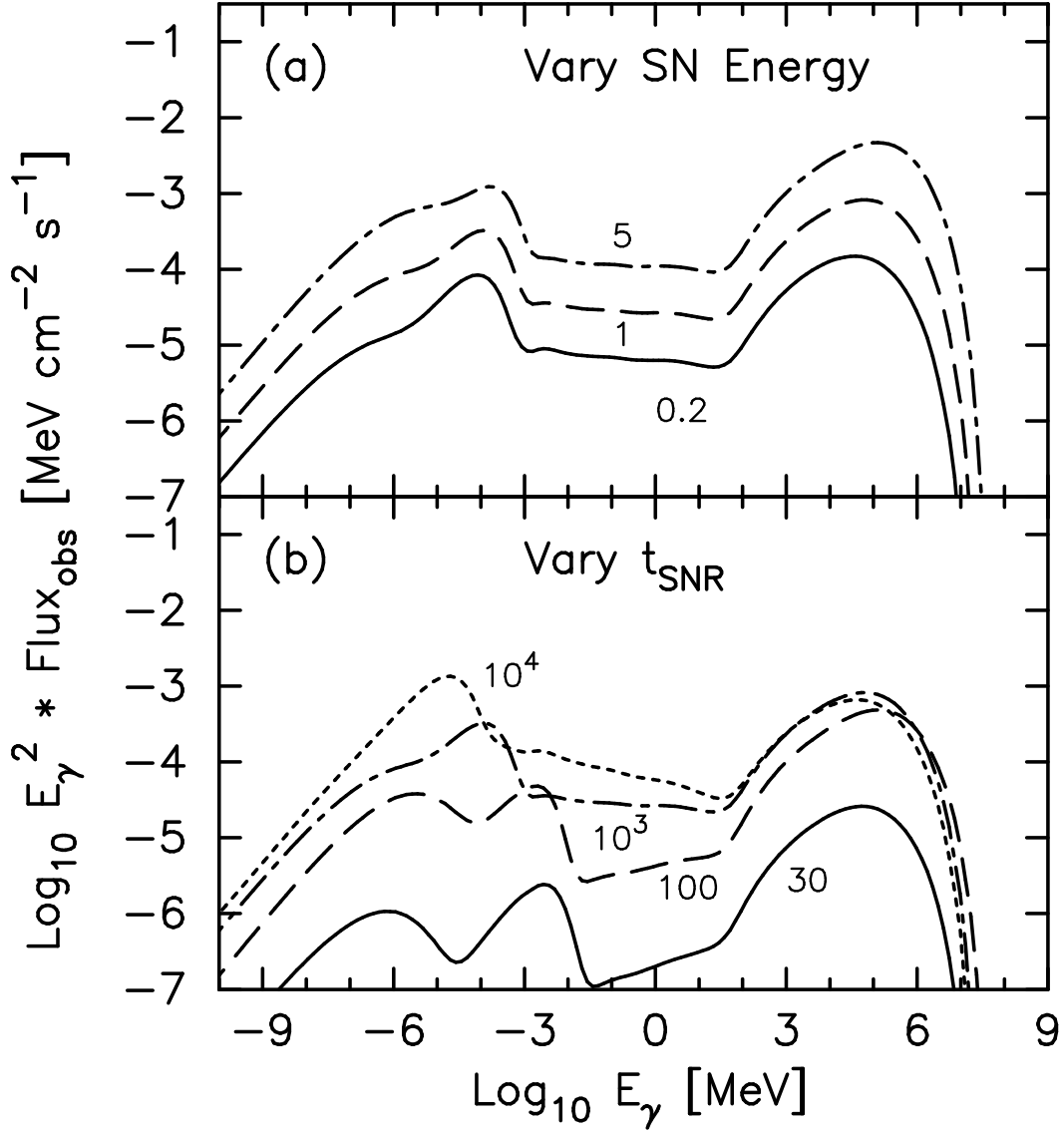


Fig. 6.— Total photon emission for various input parameters. In (a), $E_{\text{sn}} = 0.2 \times 10^{51}$ erg (solid), 1×10^{51} erg (dashed), and 5×10^{51} erg (dot-dashed). In (b), $t_{\text{snr}} = 30$ yr (solid), 100 yr (dashed), 10^3 yr (dot-dashed), and 10^4 yr (dotted). In all cases, $\eta_{\text{inj,p}} = 10^{-3}$, $n_{p0} = 1 \text{ cm}^{-3}$, $B = 3 \mu\text{G}$, $T_{e2}/T_{p2} = 1$, $(e/p)_{\text{rel}} = 0.03$, $M_{\text{ej}} = 1 M_\odot$, $\alpha = 1$, $\eta_{\text{mfp}} = 1$, and the flux at Earth is determined assuming $D_{\text{snr}} = 1$ kpc and an emission volume given by Eqn. (19).

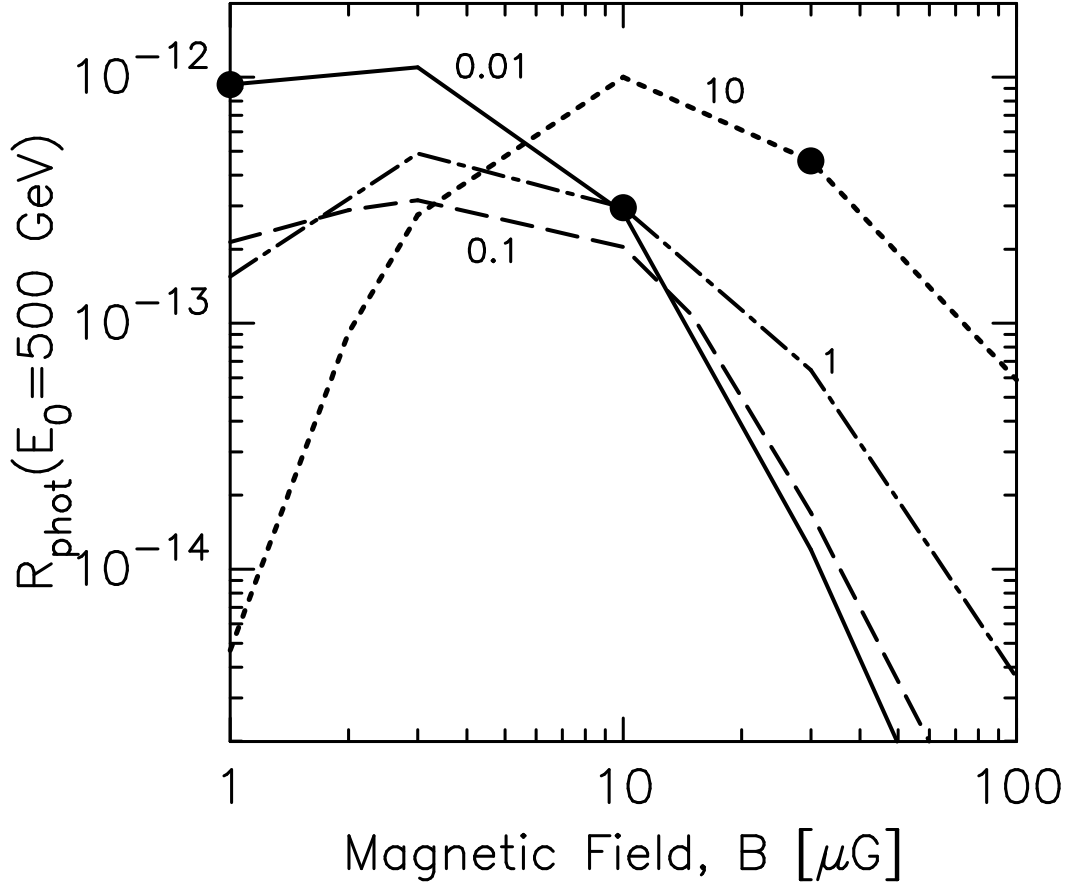


Fig. 7.— The ratio of gamma-ray to radio fluxes, R_{phot} , as defined in the text as a function of magnetic field and unshocked density as marked in cm^{-3} . All plots have $E_{\text{sn}} = 10^{51}$ erg, $M_{\text{ej}} = 1M_{\odot}$, $(e/p)_{\text{rel}} = 0.03$, $\eta_{\text{inj,p}} = 10^{-3}$, $t_{\text{snr}} = 1000$ yr, $\alpha = 1$, $\eta_{\text{mfp}} = 1$, and $T_{e2}/T_{p2} = 1$. The dots indicate parameters used in Figure 8.

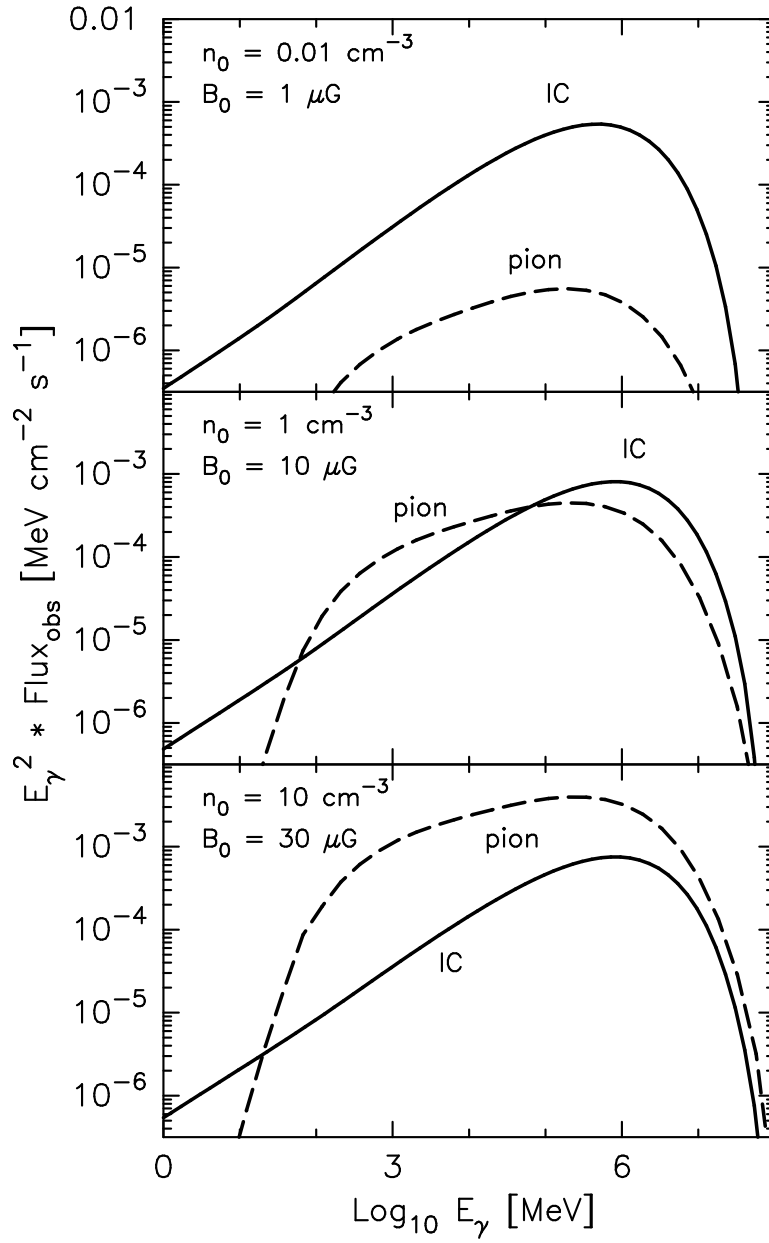


Fig. 8.— Inverse-Compton and pion-decay components for the densities and magnetic fields marked with dots in Fig. 7.

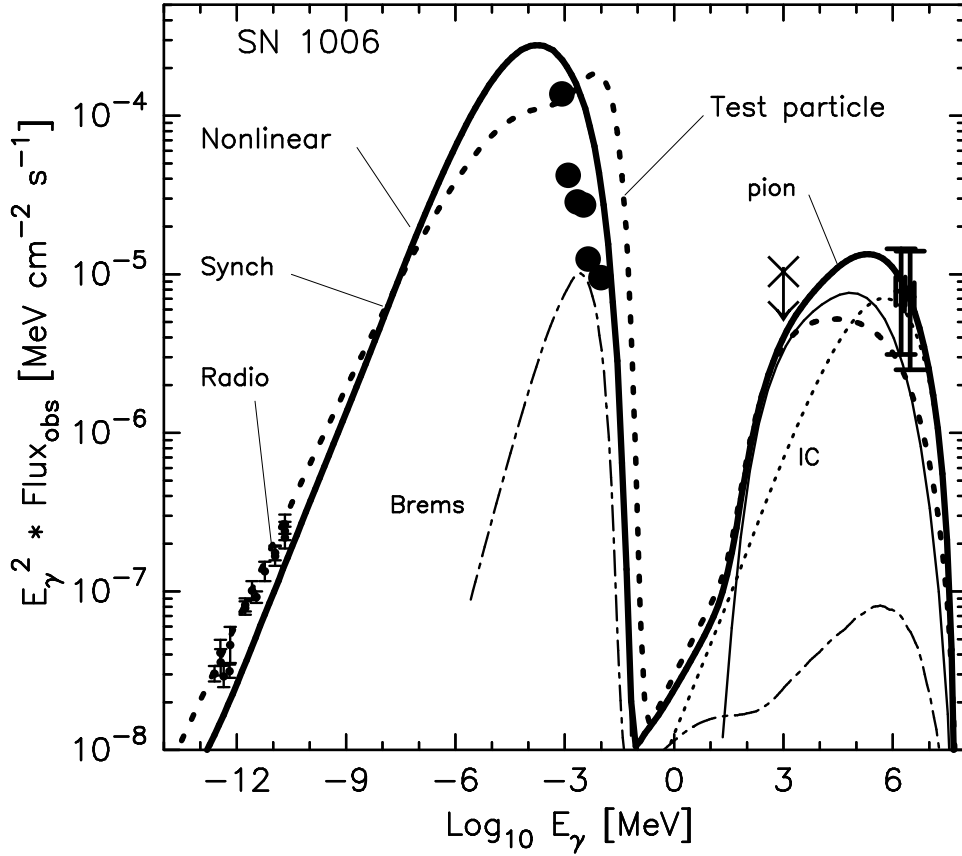


Fig. 9.— Photon spectra for SN1006. All spectra are calculated at the shock and show a ‘snapshot’ of the remnant at 990 yr after the explosion. The heavy-weight solid and dotted curves are sums of the four photon components. The component spectra for the heavy-weight solid curve are shown and labeled. The heavy solid curve is the result for a nonlinear shock, while the heavy dotted curve is a test-particle result. The radio data are from Reynolds & Ellison (1992) and the X-ray data (solid points) are adapted from Reynolds (1996), the EGRET upper limit (cross) is from Mastichiadis & de Jager (1996), and the CANGAROO TeV points (squares) are from Tanimori et al.(1998). Note that the integral CANGAROO points are plotted, with no adjustment, on our differential representation.

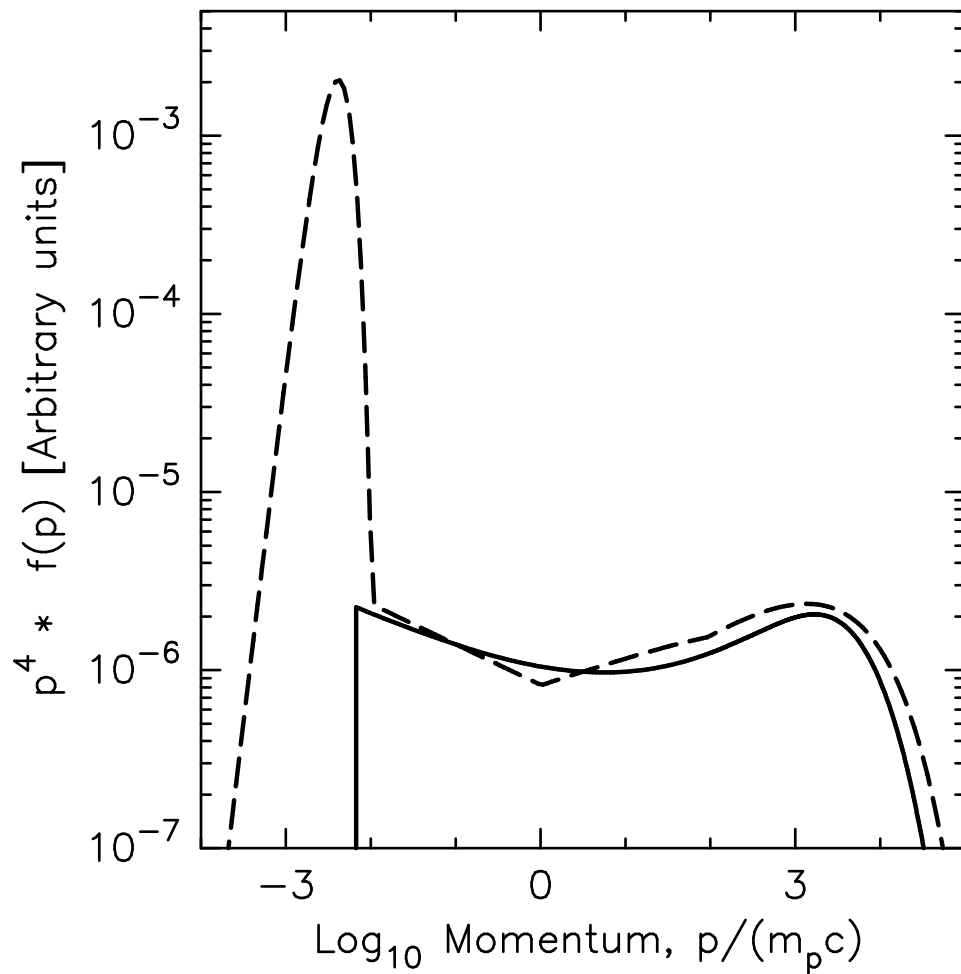


Fig. 10.— Proton phase space distributions from the simple model calculated here (dashed line) and the kinetic model of Berezhko, Ksenofontov, & Petukhov (1999a) (solid line) for SN1006. The Berezhko et al. result is the solid curve in their Figure 1d, and no adjustment in normalization is made to improve the match.

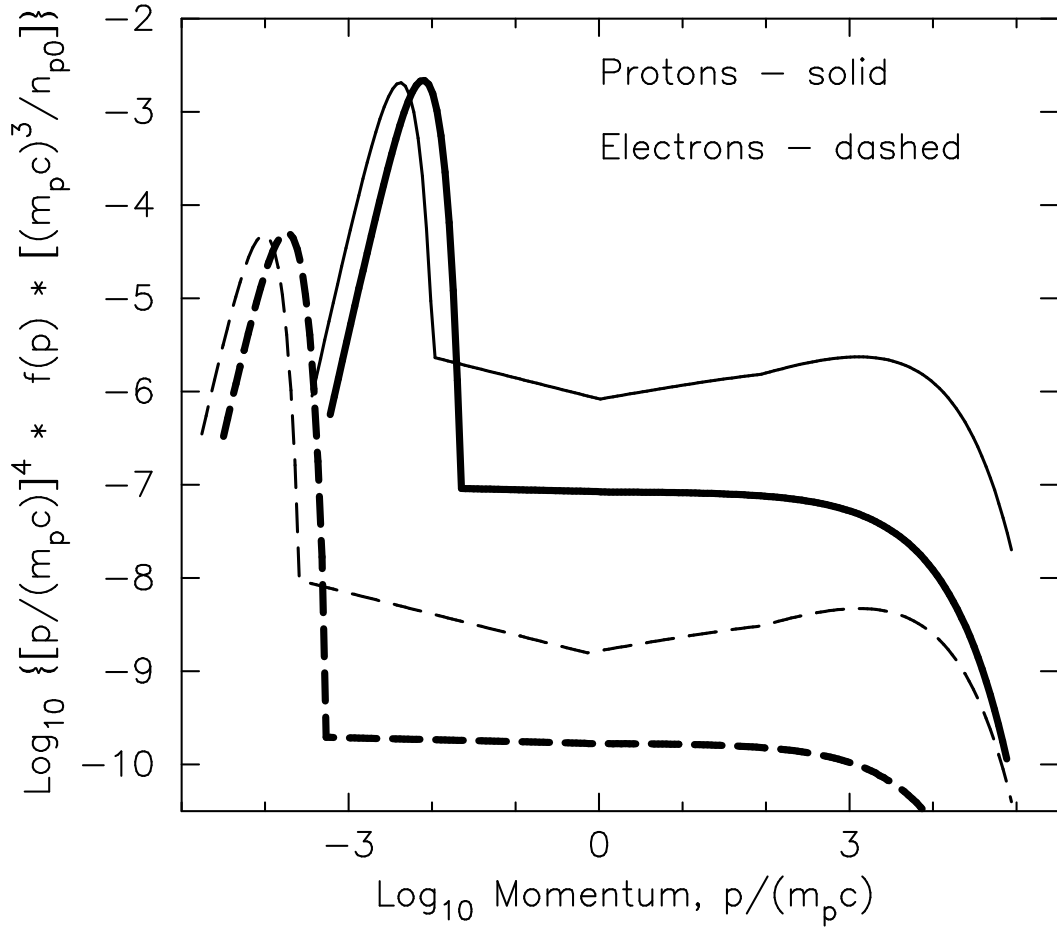


Fig. 11.— Electron and proton phase space distributions for the nonlinear and test-particle models shown in Fig. 9. The light-weight curves show the nonlinear $f(p)$, while the heavy-weight curves show the test-particle $f(p)$. All input parameters, other than the proton injection efficiency, are the same in the two cases. Compared to the nonlinear result, the test-particle example has a higher shocked temperature (as indicated by the position of the thermal peak) and a lower shocked density. The difference in density is not apparent from the figure because of the normalization.